Advances in Shell Finite Elements

Session Organizer: Christopher EARLS (Cornell University)

Keynote Lecture
Stressing thermo-mechanical analysis of FGM shells
J.N. REDDY (Texas A & M), Román A. ARCINIEGA (ABAQUS)*

An investigation of the isogeometric approach from the viewpoint of finite element technology
Ralph ECHTER, Manfred BISCHOFF (University of Stuttgart)*

Locking-free formulation for the stabilized enhanced strain solid-shell element (SHB8PS): Geometrically non-linear applications
Farid ABED-MERAIM (LPMM), Alain COMBESCURE (LaMCoS)*

New prismatic solid-shell element: Assumed strain formulation and evaluation of benchmark problems
Vuong-Dieu TRINH, Farid ABED-MERAIM (LPMM), Alain COMBESCURE (LaMCoS)*

Evolution of the new rotation-free finite element shell triangle using accurate geometrical data
*Pere-Andreu UBACH *, Eugenio OÑATE (CIMNE, UPC)*

New curvature formulation of the SFE rotation-free shell element
Sylvain COUËDO, Laëtitia DUIGOU, Gérard RIO (LIMATB, UBS)*

Largest geometrically exact nonlinear thin beam, plate & shell elements and c-type FEM
Debabrata RAY (Institute for Dynamic Response, Inc.)

A new shell element for elasto-plastic finite strain analysis: Application to the collapse and post-collapse analysis of marine pipelines
Rita TOSCANO (University of Buenos Aires), Eduardo DVORKIN (SIM&TEC)*

A finite element analysis of axially crushed corrugated frusta
Mahmoud M. A. YOUNES (M.T.C. Cairo)

For multiple-author papers:
Contact author designated by *
Presenting author designated by underscore

Proceedings of the 6th International Conference on
Computation of Shell and Spatial Structures
IASS-IACM 2008: "Spanning Nano to Mega"
28-31 May 2008, Cornell University, Ithaca, NY, USA
John F. ABEL and J. Robert COOKE (eds.)

Stressing thermo-mechanical analysis of FGM shells

J.N. REDDY* and Román A. ARCINIEGA

*Department of Mechanical Engineering, Texas A&M University
College Station, TX 77843-3123, USA

Abstract

In this lecture, a stressing thermo-mechanical model of functionally graded material plates and shells is presented. In particular, the mechanical and thermal bending analysis as well as buckling of functionally graded shells is discussed. The formulation is based on the first-order shear deformation theory of shells [1, 2]. A displacement finite element model of is developed using C^0 continuity and a family of high-order Lagrange interpolation functions is used to avoid shear locking. Several examples and applications involving FGM shells are presented at the end of the presentation.

References

[1]. R.A. Arciniega, J.N. Reddy, Consistent third-order shell theory with application to composite circular cylinders, AIAA J. 43 (9) (2005) 2024-2038.

[2]. J.N. Reddy, R.A. Arciniega, Shear deformation plate and shell theories: From Stavsky to present, Mech. Advanced Mater. Struct. 11 (2004) 535-582.

[3]. J.N. Reddy and R.A. Arciniega, "Mechanical and Thermal Buckling of Functionally Graded Ceramic-Metal Plates," *Analysis and Design of Plated Structures (Volume 1: Stability)*, Ed.: N.E. Shanmugam and C.M. Wang, Woodhead Publishing Limited, ISBN 1 85573 967 4, 2006.

Proceedings of the 6th International Conference on
Computation of Shell and Spatial Structures
IASS-IACM 2008: "Spanning Nano to Mega"
28-31 May 2008, Cornell University, Ithaca, NY, USA
John F. ABEL and J. Robert COOKE (eds.)

An investigation of the isogeometric approach from the viewpoint of finite element technology

Ralph ECHTER*, Manfred BISCHOFF

*Institut für Baustatik und Baudynamik, Universität Stuttgart
Pfaffenwaldring 7, D-70550 Stuttgart, Germany
echter@ibb.uni-stuttgart.de

Abstract

The properties of discretization schemes using NURBS for both geometry and displacements ("isogeometric approach") are investigated in the context of three-dimensional analysis of thin shells. Element behavior with respect to locking problems which are typical for shells is investigated and convergence rates are compared to those of classical finite element approaches. The study represents research in progress, focusing on the basic features of the isogeometric concept from the viewpoint of finite element technology, rather than investigating sophisticated shell problems.

1. Introduction

Analysis of shell structures with the finite element method has been in the focus of research since the development of FEM in the middle of the last century. The persisting interest in efficient and reliable analysis methods for shells is motivated by their practical importance but also by the challenge of overcoming the particular difficulties coming along with modeling and analysis of thin-walled structures.

One of the most prominent problems is the effect of *locking*, coming along in numerous different shapes in the context of shells. Locking leads to an underestimation of the displacements, and is typically accompanied by oscillating stresses or stress resultants. The mathematical reason is the fact that a stiff differential equation has to be solved. The most important locking effects for shells are

- Transverse shear locking,
- Membrane locking and
- Curvature thickness locking (trapezoidal locking).

Transverse shear locking is related to the effect of transverse shear strains and therefore it is not an issue when Kirchhoff-Love type finite elements are used. Membrane locking does only appear for curved elements. It is therefore almost insignificant if (bi-) linear shell elements are used but it is particularly pronounced for quadratic elements. Curvature thickness locking emanates from parasitic transverse normal stresses and therefore does only appear in three-dimensional shell formulations. Common features of all these locking effects is that they lead to parasitic stresses and thus artificial stiffness in the case of pure bending and that the locking phenomenon becomes more pronounced as the shell gets thinner.

When thin shells are modeled with three-dimensional continuum elements (3d-solids, "bricks"), all these locking effects are present as well, i.e. modeling shells with solid elements is conceptually simple but at the same time the worst case scenario in terms of finite element technology. As the standard elasticity equations, instead of the equations emanating from a certain shell theory, are solved when this strategy is used, the mathematical reason for locking – solving a stiff differential equation – has apparently vanished. The reason for the ill-conditioning (locking) is now the fact that the computational domain is thin.

Many different concepts to avoid locking, like reduced integration and multi-field finite element methods have been developed. There is, however, no low order formulation known to the authors which avoids all the aforementioned locking effects and passes the constant strain patch test at the same time.

Alternatively, using higher order elements is an easy way to avoid locking. In this paper, a particular version of higher order elements, based on shape functions using NURBS is investigated with respect to its convergence properties, particularly in view of the aforementioned locking effects.

2. NURBS finite elements and the isogeometric approach

In the field of CAD/ CAM application of NURBS is quite popular because of the possibility to exactly represent arbitrary analytic geometries as well as free-form shapes [1,2]. Recently, the idea of applying NURBS also for approximation of displacement fields within numerical approximation methods for problems in structural mechanics has experienced a renaissance in the so-called *isogeometric* approach [3]. The idea is to use NURBS within an *iso*parametric finite element concept thus having an exact representation of geometry which enables mesh refinement to any level without requiring further interaction to CAD systems. Computation of the element stiffness matrices and the formation of the global stiffness matrix follow the same procedure as for conventional finite elements. For numerical integration Gauss quadrature is used in the present study.
NURBS basis functions are a generalization of non-rational B-spline basis functions. They may be defined recursively by using the Cox-de Boor formulas starting with piecewise constants

$$N_{i,0}(t) = \begin{cases} 1 & for\ t_i \leq t < t_{i+1} \\ 0 & otherwise \end{cases} \tag{1}$$

and subsequently adding

$$N_{i,p}(t) = \frac{(t-t_i)*N_{i,p-1}(t)}{t_{i+p}-t_i} + \frac{(t_{i+p+1}-t)*N_{i+1,p-1}(t)}{t_{i+p+1}-t_{i+1}} \tag{2}$$

where t is the parametric variable [3]. Rational B-spline entities are obtained by projective transformation of the non-rational B-spline data set. In one dimension a knot vector $\boldsymbol{T}$ consists of $n+p+1$ knot values t_i which are the coordinates in the parametric space, where p is the polynomial degree, and n is the number of B-spline basis functions. Two dimensional basis functions are calculated by the tensor product of the basis functions of the biparametric t_1 and t_2 directions which can analogously be extended to three dimensional cases [1], [2], [3].

Important properties of NURBS and the application of NURBS basis functions for the analysis of problems described by partial differential equations as e.g. structural mechanics, fluid mechanics or electromagnetics respectively are among others described in [1], [2], [3], [4], [5], [6]. For the present study, two specific features of the isogeometric approach are of interest:

1. Higher order shape functions may be used within a hierarchic concept and
2. inter-element continuity may be arbitrarily chosen from C^0 up to order C^{p-1}.

The second property is a major difference to standard higher order finite elements and the question arises whether higher order continuity would provide an advantage in the approximation of smooth solutions. A higher convergence *rate* may in general not be expected, but the corresponding *absolute* error (i.e. the constant in the standard error estimate) may well be smaller. Without delving into mathematical error analysis we want to investigate this issue experimentally in the next section.

3. Numerical experiment

The three predominant locking effects mentioned in Section 1 are particularly pronounced for the case of pure bending of a curved structure. We therefore investigate the case of a cylinder subject to two opposite line loads, as shown in Figure 1. Assuming the cylinder to be infinitely long allows reduction of the problem to two dimensions (“pinched ring problem”), significantly reducing the numerical effort. As all locking effects are present already in this simple setup, generality is not compromised. In order to avoid the singularity under the concentrated load it is applied as a distributed shear force p along the cross section of the cylinder (Figure 1).

Using symmetry, one quarter of the structure is discretized. In all analyses, a quadratic approximation is used in thickness direction. This is the minimum requirement for an asymptotically correct model – a linear approxima-

tion is unable to correctly represent bending. In circumferential direction both the polynomial degree and the number of elements are varied up to a polynomial degree of four and 256 elements, respectively.

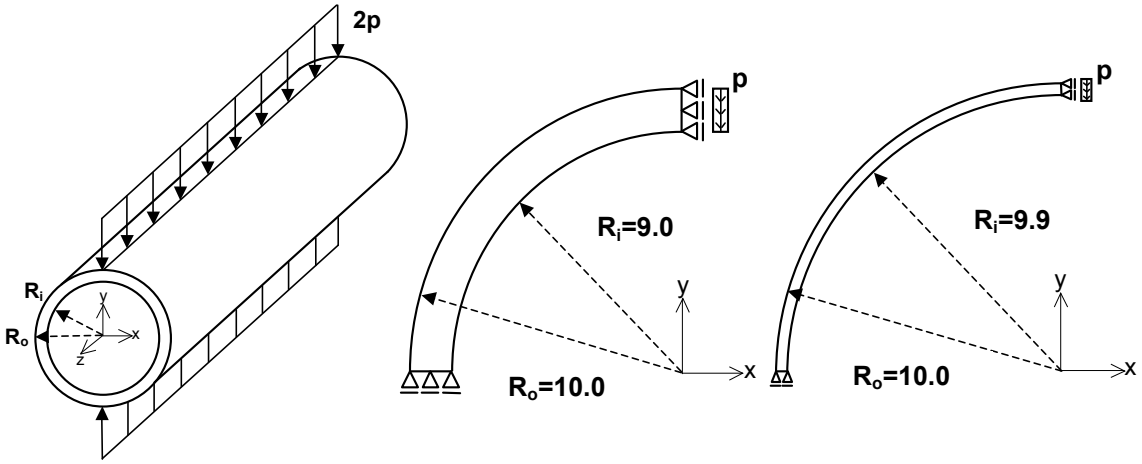

Figure 1: Pinched cylinder, problem setup

While increasing the number of elements for a fixed polynomial order we compare two different strategies:

1. *k*-refinement [3]: elevating the polynomial degree to a desired order first followed by inserting interior knots of multiplicity equal to one thus obtaining the maximum available continuity (C^{p-1} for polynomials of order p, solid lines in Figure 3), and
2. *p*-refinement: increasing the multiplicity of interior knots up to the present polynomial order followed by elevating the polynomial degree enforcing C^0-continuity at each element interface (dashed lines in Figure 3). This corresponds to *p*-refinement in the classical finite element context and the numerical results are identical to those obtained with standard isoparametric finite elements of order p.

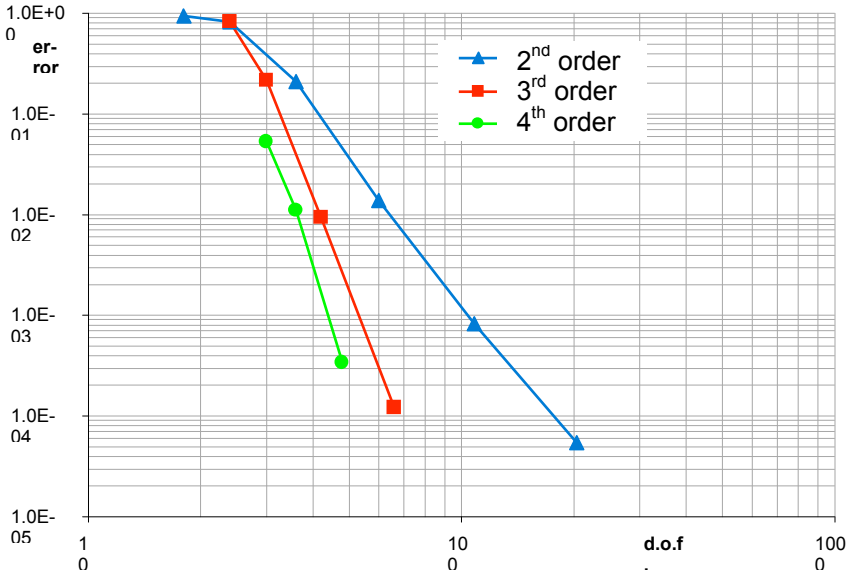

Figure 2: Thick cylinder, comparison of 2nd, 3rd and 4th order isogeometric approximations

Figure 2 shows the relative error of the C^{p-1}-continuous approach (computed with respect to a numerically obtained reference solution) for a relatively thick cylinder (R/t=10), where locking is still moderate, plotted versus the number of degrees of freedom in a log-log scale. The results show the expected behavior: Order of convergence increases with polynomial order and higher order base functions provide smaller errors for the same num-

ber of degrees of freedom. The error of the 4th order version is relatively small already for the coarsest mesh, an indication of a "completely locking-free" behavior. Because of the extremely small error for the 4th order scheme the numbers are already a deteriorated by round-off errors and the corresponding curve does not show the optimal slope. For the same reason, the 4th order results are omitted in Figure 3.

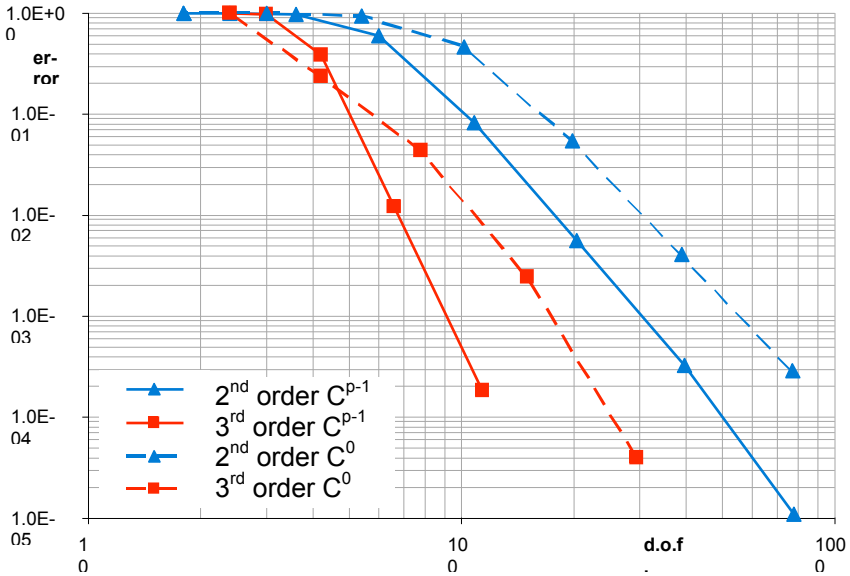

Figure 3: Thin cylinder, comparison of different continuity for 2nd and 3rd order approximations

Figure 3 shows the results of a thin cylinder problem (R/t=100) and demonstrates the superiority of the C^{p-1}-approach to the C^0-version. While asymptotic convergence rates are identical, the absolute errors are smaller when higher continuity is ensured. It is also remarkable that in each version locking occurs up to order 3! For a reference displacement of 1.0 the results for the coarsest meshes are 0.0005 and 0.002 for 2nd and 3rd order approximation, respectively (regardless of continuity). The 4th order approximation, however, yields 0.93! In contrast to the 2nd and 3rd order schemes, relative accuracy of the 4th order version is practically unaffected by the slenderness of the structure (0.94 is obtained for the thick cylinder), a clear indication of locking-free behavior.

3. Conclusions

The present study demonstrates the fact that using NURBS as finite element basis functions is not only beneficial because of exact geometry representation and direct transition of geometry data from CAD systems. Higher order continuity can also significantly improve quality of the numerical results when locking occurs. It could also be seen that locking strongly affects the results not only for linear elements, but also when quadratic and cubic shape functions are used.

References

[1] L. Piegl and W. Tiller, The NURBS Book (Monographs in Visual Communication), 2nd Edition, Springer-Verlag, Berlin, 1997

[2] D.F. Rogers, An Introduction to NURBS With Historical Perspective, Academic Press, San Diego, CA, 2001

[3] T.J.R. Hughes, J.A. Cottrell, Y. Bazilevs, Isogeometric analysis: CAD, finite elements, NURBS, exact geometry, and mesh refinement, Comput. Methods Appl. Mech. Engrg. 194 (2005) 4135–4195

[4] J.A. Cottrell, A. Reali, Y. Bazilevs, T.J.R. Hughes, Isogeometric analysis of structural vibrations, Comput. Methods Appl. Mech. Engrg. 195 (2006) 5257–5296

[5] K. Höllig, Finite Element Methods with B-Splines, SIAM, Philadelpia, 2003

[6] J.A. Cottrell, T.J.R. Hughes, A. Reali, Studies of refinement and continuity in isogeometric structural analysis, Comput. Methods Appl. Mech. Engrg. 196 (2007) 4160–4183

Proceedings of the 6th International Conference on
Computation of Shell and Spatial Structures
IASS-IACM 2008: “Spanning Nano to Mega”
28-31 May 2008, Cornell University, Ithaca, NY, USA
John F. ABEL and J. Robert COOKE (eds.)

Locking-free formulation for the stabilized enhanced strain solid-shell element (SHB8PS): geometrically non-linear applications

Farid ABED-MERAIM*, Alain COMBESCURE

*LPMM UMR CNRS 7554, ENSAM CER de Metz
4 rue Augustin Fresnel, 57078 Metz, France
farid.abed-meraim@metz.ensam.fr

Abstract

In this work, a new locking-free and physically stabilized formulation of the SHB8PS solid-shell element is presented. The resulting finite element consists of a continuum mechanics shell element based on a purely three-dimensional approach. This eight-node hexahedron is integrated with a set of five Gauss points, all distributed along the “thickness” direction. Consequently, it can be used for the modeling of thin structures, while providing an accurate description of various through-thickness phenomena. The reduced integration has been used in order to prevent some locking phenomena and to increase its computational efficiency. The spurious zero-energy deformation modes due to the reduced integration are efficiently stabilized, whereas the strain components corresponding to locking modes are eliminated with a projection technique following the Enhanced Assumed Strain (EAS) method.

1. Introduction

Over the last decade, considerable progress has been made in the development of three-dimensional finite elements capable of modeling thin structures [1], [3-5], [7]. The coupling between solid and shell formulations has proven to be an interesting way to provide continuum finite element models that can be efficiently used for structural applications. These solid-shell elements have numerous advantages for the analysis of various complex structural geometries that are common in many industrial applications. Their main advantage is to allow such complex structural shapes to be meshed without classical problems of connecting zones meshed with different element types (continuum and structural elements for instance). Another important benefit of the solid-shell concept is the avoidance of tedious and complex pure-shell element formulations needed for the complex treatment of large rotations.

In this work, a new locking-free formulation for the SHB8PS solid-shell element is performed. Note that the SHB8PS element was first implemented into the dynamic explicit finite element code (Europlexus) for impact problem simulations (Abed-Meraim and Combescure [1]). Later, an implicit version was implemented into the quasi-static implicit code (Inca) for stability analysis of shells (Legay and Combescure [4]). This element is an eight-node, three-dimensional hexahedron with a preferential direction called “the thickness”. Therefore, it can be used to represent thin structures while providing an accurate description of various through-thickness phenomena thanks to the use of a numerical integration with five Gauss points in that direction. As a result, the element is under-integrated and requires a stabilization procedure to control the associated hourglass modes. The stabilization technique used is based on the Assumed Strain Method (Belytschko and Bindeman [2]).

More specifically, this work focuses on the elimination of the residual membrane and shear locking persisting in the previous formulations. By using orthogonal projections of the discrete gradient operator, these severe shear and membrane locking modes are removed. Several numerical experiments on popular linear and non-linear benchmark problems show that this new formulation of the SHB8PS element is effective under non-linear conditions and demonstrates good convergence without locking phenomena.

2. Formulation of the SHB8PS element

The element coordinates x_i and displacements u_i $(i = 1,...,3)$ are interpolated using the isoparametric trilinear shape functions $N_I(\xi,\eta,\zeta)$ $(I = 1,...,8)$. By introducing the *Hallquist* vectors ($\underline{b}_i$, i = 1,..., 3), defined as:

$$\underline{b}_i^T = \underline{N}_{,i}(0,0,0) \qquad i = 1,2,3 \qquad \textit{Hallquist's Form} \tag{1}$$

where $\underline{N}_{,i} = \partial \underline{N} / \partial x_i$, one can show that the discrete gradient operator, which relates the linear deformations to the nodal displacements (i.e., $\underline{\underline{\nabla}}_S(\underline{u}) = \underline{\underline{B}} \cdot \underline{d}$), is given by equation (3) below. This $\underline{\underline{B}}$-matrix makes use of the following variables:

$$\begin{cases} \underline{\gamma}_\alpha = \frac{1}{8}\left[\underline{h}_\alpha - \sum_{j=1,3} (\underline{h}_\alpha^T \cdot \underline{x}_j)\underline{b}_j \right] \\ h_1 = \eta\zeta,\ h_2 = \zeta\xi,\ h_3 = \xi\eta,\ h_4 = \xi\eta\zeta \end{cases}; \quad \begin{cases} \underline{d}_i^T = (u_{i1}, u_{i2}, u_{i3}, ..., u_{i8}), & \underline{x}_i^T = (x_{i1}, x_{i2}, x_{i3}, ..., x_{i8}) \\ \underline{h}_1^T = (1,1,-1,-1,-1,-1,1,1), & \underline{h}_2^T = (1,-1,-1,1,-1,1,1,-1) \\ \underline{h}_3^T = (1,-1,1,-1,1,-1,1,-1), & \underline{h}_4^T = (-1,1,-1,1,1,-1,1,-1) \end{cases} \tag{2}$$

$$\underline{\underline{B}} = \begin{bmatrix} \underline{b}_x^T + h_{\alpha,x}\underline{\gamma}_\alpha^T & \underline{0} & \underline{0} \\ \underline{0} & \underline{b}_y^T + h_{\alpha,y}\underline{\gamma}_\alpha^T & \underline{0} \\ \underline{0} & \underline{0} & \underline{b}_z^T + h_{\alpha,z}\underline{\gamma}_\alpha^T \\ \underline{b}_y^T + h_{\alpha,y}\underline{\gamma}_\alpha^T & \underline{b}_x^T + h_{\alpha,x}\underline{\gamma}_\alpha^T & \underline{0} \\ \underline{0} & \underline{b}_z^T + h_{\alpha,z}\underline{\gamma}_\alpha^T & \underline{b}_y^T + h_{\alpha,y}\underline{\gamma}_\alpha^T \\ \underline{b}_z^T + h_{\alpha,z}\underline{\gamma}_\alpha^T & \underline{0} & \underline{b}_x^T + h_{\alpha,x}\underline{\gamma}_\alpha^T \end{bmatrix} \left(\begin{array}{l} \text{The convention of implied summation} \\ \text{of repeated subscripts } \alpha \text{ is adopted} \end{array} \right) \tag{3}$$

Despite the geometry of the element (eight-node hexahedron), several modifications are introduced in order to provide it with shell features. Among them, a shell-like behavior is intended for the element, by modifying the three-dimensional elastic constitutive law so that the plane-stress conditions are approached and by aligning all the integration points along a privileged direction, called the thickness. The stiffness matrix is then obtained by Gauss integration:

$$\underline{\underline{K}}_e = \int_{\Omega_e} \underline{\underline{B}}^T \cdot \underline{\underline{C}} \cdot \underline{\underline{B}}\, dv = \sum_{I=1}^{5} \omega(\zeta_I) J(\zeta_I) \underline{\underline{B}}^T(\zeta_I) \cdot \underline{\underline{C}} \cdot \underline{\underline{B}}(\zeta_I) \tag{4}$$

Because the $h_{\alpha,i}$ functions $(\alpha = 3,4;\ i = 1,2,3)$ vanish at the five Gauss points, of coordinates $\xi_I = \eta_I = 0,\ \zeta_I \neq 0$, the $\underline{\underline{B}}$-matrix in equation (3) reduces to its $\underline{\underline{B}}_{12}$ part, with only the $h_{\alpha,i}$ terms $(\alpha = 1,2;\ i = 1,2,3)$. This leads to six hourglass modes generated by $\underline{h}_3$ and $\underline{h}_4$. These spurious modes are stabilized following the approach given in Belytschko and Bindeman [2]. Moreover, we apply an assumed strain method in order to eliminate locking. The $\underline{\underline{B}}$-matrix is thus projected onto $\overline{\underline{\underline{B}}}$ as:

$$\overline{\underline{\underline{B}}} = \underline{\underline{B}}_{12} + \overline{\underline{\underline{B}}}_{34} \tag{5}$$

Consequently, the stiffness matrix, equation (4), can be rewritten as:

$$\underline{\underline{K}}_e = \underline{\underline{K}}_{12} + \underline{\underline{K}}_{STAB} \tag{6}$$

The first term $\underline{\underline{K}}_{12}$ is obtained by Gauss integration, equation (4). The second term $\underline{\underline{K}}_{STAB}$ represents the stabilization stiffness:

$$\underline{\underline{K}}_{STAB} = \int_{\Omega_e} \underline{\underline{B}}_{12}^T \cdot \underline{\underline{C}} \cdot \overline{\underline{\underline{B}}}_{34} dv + \int_{\Omega_e} \overline{\underline{\underline{B}}}_{34}^T \cdot \underline{\underline{C}} \cdot \underline{\underline{B}}_{12} dv + \int_{\Omega_e} \overline{\underline{\underline{B}}}_{34}^T \cdot \underline{\underline{C}} \cdot \overline{\underline{\underline{B}}}_{34} dv \tag{7}$$

3. Numerical results and discussions

The performance of this new formulation has been tested through a variety of linear and non linear mechanical problems. In all of these tests, the new version showed better performance than the previous formulation. In particular, the improvement is significant in the pinched hemispherical shell test.

3.1 Pinched hemispherical shell problem

This test has become very popular and it is used by many authors. It is severe since the shear and membrane locking phenomena are very important and emphasized by the problem geometry (distorted, skewed elements). As reported by many authors, in this doubly-curved shell problem, the membrane locking is much more severe than shear locking. Figure 1 shows the geometry, loading and boundary conditions for this problem.

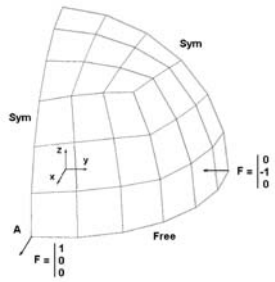

Figure 1: Geometry and loading of the pinched hemispherical shell problem

The radius is R=10, the thickness t=0.04, Young's modulus E=6.825×10^7 and Poisson's ratio ν =0.3. Using the symmetry, only a quarter of the hemisphere is meshed using a single element through the thickness and with two unit loads along directions Ox and Oy. The reference solution for the radial displacement at the load point is 0.0924. The convergence results are reported in Table 1 in terms of the normalized displacement at the load point. The new version of the SHB8PS element is compared with the former one and with the three elements HEX8, HEXDS and H8-ct-cp. The HEX8 element is the standard, eight-node, full integration solid element (eight Gauss points). The HEXDS element is an eight-node, four-point quadrature solid element (Liu *et al.* [6]). The H8-ct-cp element was developed by Lemosse [5]. Table 1 shows that the new version of the SHB8PS element provides an excellent convergence rate and shows no locking.

Number of	SHB8PS previous version	HEX8	HEXDS	H8-ct-cp	SHB8PS new version
	Ux/Uref	Ux/Uref	Ux/Uref	Ux/Uref	Ux/Uref
12	0.0629	0.0005		0.05	0.8645
27	0.0474	0.0011			1.0155
48	0.1660	0.0023	0.408	0.35	1.0098
75	0.2252	0.0030	0.512	0.58	1.0096
192	0.6332	0.0076	0.701	0.95	1.0008
363	0.8592	0.0140	0.800		1.0006
768	0.9651	0.0287			1.0006
1462	0.9910	0.0520			1.0009

Table 1: Normalized displacement at the load point of the pinched hemispherical shell

3.2 Pinched cylinder with end diaphragms

A cylindrical shell loaded by a pair of concentrated vertical forces at its middle section is considered here. Both ends of the cylinder are covered with rigid diaphragms that allow displacement only in the axial direction (Figure 2). This test is considered as a selective test problem since it has been shown that shear locking is more severe than membrane locking. The length is L=600, the radius R=300, the thickness t=3, Young's modulus

E=3×10^6, Poisson's ratio ν =0.3 and the applied load P=1. Owing to symmetry, only one eighth of the cylinder is modeled using a single element through the thickness and 2×2, 4×4, 8×8, 16×16 and 32×32 meshes: Figure 2.

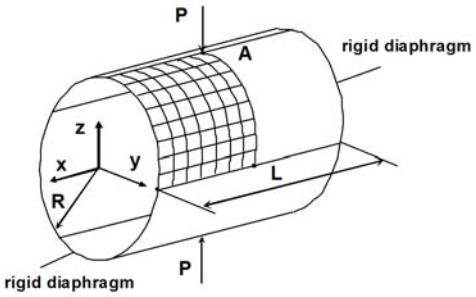

Figure 2: Geometry, boundary conditions and loading for the pinched cylinder

The displacement at the loaded point in the loading direction is normalized with respect to the reference solution of 0.18248×10^{-4} and reported in Table 2 below.

	SHB8PS previous version	SHB8PS new version
Mesh layout	Uz/Uref	Uz/Uref
2x2	0.043	0.101
4x4	0.223	0.387
8x8	0.708	0.754
16x16	0.937	0.940
32x32	0.996	0.997

Table 2: Normalized displacements at the loaded point of the pinched cylinder

As we can see in Table 2, the new version of the SHB8PS element performs better than the former one, especially for coarse meshes. This new version has also been tested on a variety of non linear, elastic and elastic-plastic problems. We demonstrate that the projection adopted in this formulation better eliminates the locking phenomena. As shown particularly in the pinched hemisphere test problem, Table 1, this element also exhibits excellent efficiency and convergence through numerous other tests.

References

[1] Abed-Meraim F and Combescure A. SHB8PS a new adaptive, assumed-strain continuum mechanics shell element for impact analysis. *Computers & Structures* 2002; **80**:791-803.

[2] Belytschko T and Bindeman LP. Assumed strain stabilization of the eight node hexahedral element. *Computer Methods in Applied Mechanics and Engineering* 1993; **105**:225-260.

[3] Hauptmann R and Schweizerhof K. A systematic development of solid-shell element formulations for linear and non-linear analyses employing only displacement degrees of freedom. *International Journal for Numerical Methods and Engineering* 1998; **42**:49-69.

[4] Legay A and Combescure A. Elastoplastic stability analysis of shells using the physically stabilized finite element SHB8PS. *International Journal for Numerical Methods and Engineering* 2003; **57**:1299-1322.

[5] Lemosse D. Eléments finis iso-paramétriques tridimensionnels pour l'étude des structures minces. PhD Thesis, Ecole Doctorale SPMI/INSA-Rouen, 2000.

[6] Liu WK, Guo Y, Tang S and Belytschko T. A multiple-quadrature eight-node hexahedral finite element for large deformation elastoplastic analysis. *Comp. Meth. in Applied Mech. and Engng.* 1998; 154:69-132.

[7] Wall WA, Bischoff M and Ramm E. A deformation dependent stabilization technique, exemplified by EAS elements at large strains. *Computer Methods in Applied Mechanics and Engng.* 2000; **188**:859-871.

Proceedings of the 6th International Conference on
Computation of Shell and Spatial Structures
IASS-IACM 2008: "Spanning Nano to Mega"
28-31 May 2008, Cornell University, Ithaca, NY, USA
John F. ABEL and J. Robert COOKE (eds.)

New prismatic solid-shell element: Assumed strain formulation and evaluation on benchmark problems

Vuong-Dieu TRINH*, Farid ABED-MERAIM, Alain COMBESCURE

*LPMM UMR CNRS 7554, ENSAM CER de Metz, 4 rue Augustin Fresnel, 57078 Metz, France
*LaMSID UMR EDF/CNRS 2832, EDF R&D, 1 avenue du General de Gaulle, 92141 Clamart Cedex, France
vuong-dieu.trinh@metz.ensam.fr, vuong-dieu.trinh@edfgdf.fr, farid.abed-meraim@metz.ensam.fr

Abstract

This paper presents the development of a six-node solid-shell finite element called (SHB6) and based on the assumed strain method adopted by Belytschko *et al.* [2]. It is integrated with a set of five Gauss points along a special direction, denoted "thickness", and with only one point in the other in-plane directions. Its discrete gradient is modified in order to attenuate shear and membrane locking. A series of popular linear benchmark problems has been carried out with comparisons to geometrically similar, low-order three-dimensional elements.

1. Introduction

Accuracy and efficiency are the main features expected in finite element methods. In three-dimensional analysis of structural problems, the development of effective eight-node solid-shell finite elements has been a major objective over the last decade as testified by many recently published contributions [1-5]. However, to be able to mesh complex geometries and with the advent of free mesh generation tools not generating only hexahedrons, the development of prismatic elements is made necessary. This paper presents the formulation of a six-node solid-shell finite element called SHB6. It represents a thick shell obtained from a purely three-dimensional approach. The assumed strain method is adopted together with an in-plane reduced integration scheme with five Gauss points along the thickness direction. The three-dimensional elastic constitutive law is also modified so that a shell-like behavior is intended for the element and in order to alleviate shear and membrane locking.

Because the reduced integration is known to introduce spurious modes associated with zero energy, an adequate hourglass control is generally needed as proposed by Belytschko *et al.* [2] with a physical stabilization procedure to correct the rank deficiency of eight-node hexahedral elements. As the SHB6 is also under-integrated, a detailed eigenvalue analysis of the element stiffness matrix is carried out. We demonstrate that the kernel of this stiffness matrix only reduces to rigid body movements and hence, in contrast to the eight-node solid-shell element (SHB8PS), the SHB6 element does not require stabilization.

Numerical evaluations of the SHB6 element showed that its initial version, without modification of its discrete gradient operator, suffered from shear and membrane locking. To attenuate these locking phenomena, several modifications have been introduced into the formulation of the SHB6 element following the assumed strain method adopted by Belytschko *et al.* [2]. Finally, a variety of popular benchmark problems has been performed and good results have been obtained when compared to other well-established elements in the literature.

2. Formulation of the SHB6 finite element

The SHB6 finite element is a solid-shell with only three displacement degrees of freedom per node, and it has a special direction called "thickness". It is integrated with a set of five Gauss points along this direction and only one point in the in-plane directions. Figure 1 shows the SHB6 reference geometry as well as its Gauss points.

2.1 Kinematics and interpolation

The SHB6 is a linear, isoparametric element. Its spatial coordinates x_i and displacements u_i are respectively related to the nodal coordinates x_{iI} and displacements u_{iI} through the linear shape functions N_I as follows:

$$x_i = x_{iI} N_I(\xi,\eta,\zeta) = \sum_{I=1}^{6} x_{iI} N_I(\xi,\eta,\zeta) \quad \text{and} \quad u_i = u_{iI} N_I(\xi,\eta,\zeta) = \sum_{I=1}^{6} u_{iI} N_I(\xi,\eta,\zeta) \tag{1}$$

Hereafter, unless specified otherwise, the implied summation convention for repeated indices will be adopted. Lowercase indices i vary from one to three and represent spatial coordinate directions. Uppercase indices I vary from one to six and correspond to element nodes. The tri-linear isoparametric shape functions N_I are:

$$\underline{N}_I(\xi,\eta,\zeta) = \frac{1}{2}\left[(1-\zeta)(1-\xi-\eta) \quad (1-\zeta)\xi \quad (1-\zeta)\eta \quad (1+\zeta)(1-\xi-\eta) \quad (1+\zeta)\xi \quad (1+\zeta)\eta\right] \tag{2}$$
$$\xi = [0,1]; \quad \eta = [0,1-\xi]; \quad \zeta = [-1,1]$$

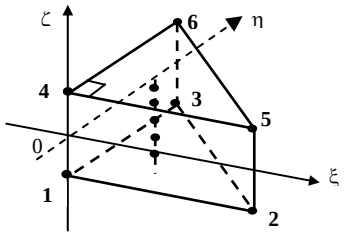

Figure 1: Reference geometry of the SHB6 element and its Gauss points

2.2 Discrete gradient operator

Using some mathematical derivations, similarly to the procedure of the SHB8PS development reported in [1], we can explicitly express the relationship between the strain field and the nodal displacements as:

$$\underline{\underline{\nabla}}_s(\underline{u}) = \begin{bmatrix} u_{x,x} \\ u_{y,y} \\ u_{z,z} \\ u_{x,y}+u_{y,x} \\ u_{x,z}+u_{z,x} \\ u_{y,z}+u_{z,y} \end{bmatrix} = \begin{bmatrix} \underline{b}_x^T + h_{\alpha,x}\underline{\gamma}_\alpha^T & \underline{0} & \underline{0} \\ \underline{0} & \underline{b}_y^T + h_{\alpha,y}\underline{\gamma}_\alpha^T & \underline{0} \\ \underline{0} & \underline{0} & \underline{b}_z^T + h_{\alpha,z}\underline{\gamma}_\alpha^T \\ \underline{b}_y^T + h_{\alpha,y}\underline{\gamma}_\alpha^T & \underline{b}_x^T + h_{\alpha,x}\underline{\gamma}_\alpha^T & \underline{0} \\ \underline{b}_z^T + h_{\alpha,z}\underline{\gamma}_\alpha^T & \underline{0} & \underline{b}_x^T + h_{\alpha,x}\underline{\gamma}_\alpha^T \\ 0 & \underline{b}_z^T + h_{\alpha,z}\underline{\gamma}_\alpha^T & \underline{b}_y^T + h_{\alpha,y}\underline{\gamma}_\alpha^T \end{bmatrix} \cdot \begin{bmatrix} \underline{d}_x \\ \underline{d}_y \\ \underline{d}_z \end{bmatrix} = \underline{\underline{B}} \cdot \underline{d} \tag{3}$$

where the h_α functions are: $h_1 = \eta\zeta$, $h_2 = \xi\zeta$; the $\underline{b}_i$ vectors are: $\underline{b}_i^T = \underline{N}_{,i}(0) = \partial \underline{N} / \partial x_i \big|_{\xi=\eta=\zeta=0}$; $i = 1,2,3$ and the constant vectors $\underline{\gamma}_\alpha$ are given by: $\underline{\gamma}_\alpha = \frac{1}{2}\left(\underline{h}_\alpha - \sum_{i=1}^{3} \left(\underline{h}_\alpha^T \cdot \underline{x}_i \right) \underline{b}_i \right)$; $\alpha = 1,2$. In this latter expression, $\underline{h}_1^T = (0, \ 0, \ -1, \ 0, \ 0, \ 1)$; $\underline{h}_2^T = (0, \ -1, \ 0, \ 0, \ 1, \ 0)$ and the $\underline{x}_i$ vectors denote the nodal coordinates. We can also demonstrate the following orthogonality conditions:

$$\underline{\gamma}_\alpha^T \cdot \underline{x}_j = 0\,, \qquad \underline{\gamma}_\alpha^T \cdot \underline{h}_\beta = \delta_{\alpha\beta} \tag{4}$$

2.3 Variational principle

Applying the simplified form of the Hu-Washizu non linear mixed variational principle, in which the assumed stress field is chosen to be orthogonal to the difference between the symmetric part of the displacement gradient and the assumed strain field, we obtain:

$$\delta\pi\left(\underline{u},\underline{\overline{\varepsilon}}\right)=\int_{V_e}\delta\underline{\overline{\varepsilon}}^{T}\cdot\underline{\sigma}\,dV-\delta\underline{d}^{T}\cdot\underline{f}^{ext}=0 \tag{5}$$

Replacing the assumed strain field, with its expression $\underline{\overline{\varepsilon}}(x,t)=\underline{\overline{B}}(x)\cdot\underline{d}(t)$, in equation (5) leads to the following expression for the internal forces:

$$\underline{f}^{\text{int}}=\int_{V_e}\underline{\overline{B}}^{T}\cdot\underline{\sigma}\left(\underline{\overline{\varepsilon}}\right)dV \tag{6}$$

This also leads to the following expression for the element elastic stiffness matrix:

$$\underline{\underline{K}}_e=\int_{V_e}\underline{\overline{B}}^{T}\cdot\underline{\underline{C}}\cdot\underline{\overline{B}}\,dV \tag{7}$$

Note that for a standard displacement approach, $\underline{\overline{B}}$ is simply replaced with $\underline{B}$ leading to the classical stiffness:

$$\underline{\underline{K}}_e=\int_{V_e}\underline{B}^{T}\cdot\underline{\underline{C}}\cdot\underline{B}\,dV \tag{8}$$

2.3 Hourglass mode analysis for the SHB6 element

Hourglass modes are spurious zero-energy modes that are generated by the reduced integration. In static problems, they may lead to singularity of the assembled stiffness matrix for certain boundary conditions; in most cases this results in spurious mechanisms also known as rank deficiencies. Therefore, the analysis of hourglass modes is equivalent to that of the stiffness matrix kernel, namely zero-strain modes $\underline{d}$ that satisfy:

$$\underline{B}\left(\zeta_{Gj}\right)\cdot\underline{d}=\underline{0}\qquad\forall\zeta_{Gj} \tag{9}$$

To this end, we can build a basis for the discretized displacements by demonstrating that the eighteen column vectors below are linearly independent. Making use of orthogonality conditions (4), we show that only the first six column vectors verify equation (9) and correspond to rigid body modes. This means that there are no hourglass modes for the SHB6 element. In other words, the SHB6 element does not require hourglass control.

$$\begin{bmatrix}
\underline{S} & \underline{0} & \underline{0} & \underline{y} & \underline{z} & \underline{0} & \underline{x} & \underline{0} & \underline{0} & \underline{y} & \underline{z} & \underline{0} & \underline{h}_1 & \underline{0} & \underline{0} & \underline{h}_2 & \underline{0} & \underline{0} \\
\underline{0} & \underline{S} & \underline{0} & -\underline{x} & \underline{0} & \underline{z} & \underline{0} & \underline{y} & \underline{0} & \underline{x} & \underline{0} & \underline{z} & \underline{0} & \underline{h}_1 & \underline{0} & \underline{0} & \underline{h}_2 & \underline{0} \\
\underline{0} & \underline{0} & \underline{S} & \underline{0} & -\underline{x} & -\underline{y} & \underline{0} & \underline{0} & \underline{z} & \underline{0} & \underline{x} & \underline{y} & \underline{0} & \underline{0} & \underline{h}_1 & \underline{0} & \underline{0} & \underline{h}_2
\end{bmatrix} \tag{10}$$

2.4 Assumed strain formulation for the SHB6 discrete gradient operator

Among several treatments for alleviating shear and membrane locking, the discrete gradient is appropriately modified. This consists first of decomposing the matrix $\underline{\underline{B}}$ into two parts: $\underline{\underline{B}}=\underline{\underline{B}}_1+\underline{\underline{B}}_2$, then of projecting the second part onto an assumed strain operator such that $\underline{\overline{B}}=\underline{B}_1+\underline{\overline{B}}_2$. As a result, the stiffness matrix becomes:

$$\underline{\underline{K}}_e=\int_{V_e}\underline{\underline{B}}_1^{T}\cdot C\cdot\underline{\underline{B}}_1\,dV+\int_{V_e}\underline{\underline{B}}_1^{T}\cdot C\cdot\underline{\overline{B}}_2\,dV+\int_{V_e}\underline{\overline{B}}_2^{T}\cdot C\cdot\underline{\underline{B}}_1\,dV+\int_{V_e}\underline{\overline{B}}_2^{T}\cdot C\cdot\underline{\overline{B}}_2\,dV=\underline{\underline{K}}_{e1}+\underline{\underline{K}}_{e2}+\underline{\underline{K}}_{e3}+\underline{\underline{K}}_{e4} \tag{11}$$

The subsequent steps consist of choosing an adequate assumed strain field. This is a key point in the formulation and special care has been exercised in this regard. Finally, the above additive decomposition of the stiffness matrix is calculated using a reduced integration scheme with five Gauss points. Note that the choice of an assumed strain field is mainly guided by the elimination of strain components that are responsible for shear as well as membrane locking. The advantages of this enhanced strain will be shown through benchmark problems.

$$\underline{\underline{B}}_1 = \begin{bmatrix} \underline{b}_x^T + h_{\alpha,x}\underline{\gamma}_\alpha^T & \underline{0} & \underline{0} \\ \underline{0} & \underline{b}_y^T + h_{\alpha,y}\underline{\gamma}_\alpha^T & \underline{0} \\ \underline{0} & \underline{0} & \underline{b}_z^T + h_{\alpha,z}\underline{\gamma}_\alpha^T \\ \underline{b}_y^T + h_{\alpha,y}\underline{\gamma}_\alpha^T & \underline{b}_x^T + h_{\alpha,x}\underline{\gamma}_\alpha^T & \underline{0} \\ \underline{0} & \underline{0} & \underline{0} \\ 0 & \underline{0} & \underline{0} \end{bmatrix}; \quad \underline{\underline{B}}_2 = c \begin{bmatrix} \underline{0} & \underline{0} & \underline{0} \\ \underline{0} & \underline{0} & \underline{0} \\ \underline{0} & \underline{0} & \underline{0} \\ \underline{0} & \underline{0} & \underline{0} \\ \underline{b}_z^T + h_{\alpha,z}\underline{\gamma}_\alpha^T & \underline{0} & \underline{b}_x^T + h_{\alpha,x}\underline{\gamma}_\alpha^T \\ 0 & \underline{b}_z^T + h_{\alpha,z}\underline{\gamma}_\alpha^T & \underline{b}_y^T + h_{\alpha,y}\underline{\gamma}_\alpha^T \end{bmatrix}$$

3. Numerical results and comparison

Several popular benchmark problems were performed to illustrate the element performance; one of these test problems is given here. This example is frequently used in the literature to test warping effects on shell elements.

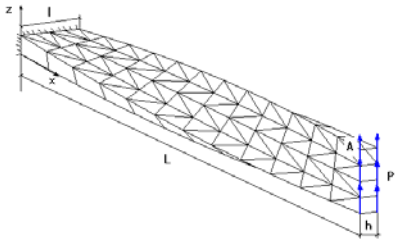

Figure 2: Twisted beam. Length =12; width = 1.1; depth = 0.32, twist = 90° (root to tip); E = $29x10^6$; ν = 0.22. Loading: unit force at tip. The reference vertical displacement of point A at tip is $5.424x10^{-3}$

Number of elements	SHB6 initial	PRI6 (3D solid element)	SHB6 with modification
96	0,470	0,202	0,784
192	0,779	0,485	0,935
384	0,810	0,612	0,968

Table 1: Normalized vertical displacement at point A of the twisted cantilever beam problem

4. Conclusions

This newly developed SHB6 element was implemented into the finite element codes INCA and ASTER. It represents some improvement since it converges relatively well and it performs better than the PRI6 six-node three-dimensional element in all of the benchmark problems tested. Furthermore, it shows very good performances in problems using mixed meshes composed of SHB6 and SHB8PS elements. Thus, we can couple the SHB6 with other finite elements to mesh complex geometries. For the remaining locking modes, exhibited in some test problems, a detailed study revealed that the transverse shear was behind these locking phenomena.

References

[1] Abed-Meraim F and Combescure A. SHB8PS a new adaptive, assumed-strain continuum mechanics shell element for impact analysis. *Computers & Structures* 2002; **80**:791-803.

[2] Belytschko T and Bindeman LP. Assumed strain stabilization of the eight node hexahedral element. *Computer Methods in Applied Mechanics and Engineering* 1993; **105**:225-260.

[3] Hauptmann R and Schweizerhof K. A systematic development of solid-shell element formulations for linear and non-linear analyses employing only displacement degrees of freedom. *International Journal for Numerical Methods and Engineering* 1998; **42**:49-69.

[4] Legay A and Combescure A. Elastoplastic stability analysis of shells using the physically stabilized finite element SHB8PS. *International Journal for Numerical Methods and Engineering* 2003; **57**:1299-1322.

[5] Wall WA, Bischoff M and Ramm E. A deformation dependent stabilization technique, exemplified by EAS elements at large strains. *Computer Methods in Applied Mechanics and Engng.* 2000; **188**:859-871.

Proceedings of the 6th International Conference on
Computation of Shell and Spatial Structures
IASS-IACM 2008: “Spanning Nano to Mega”
28-31 May 2008, Cornell University, Ithaca, NY, USA
John F. ABEL and J. Robert COOKE (eds.)

Evolution of the New Rotation-Free Finite Element Shell Triangle Using Accurate Geometrical Data

Pere-Andreu UBACH*, Eugenio OÑATE

*CIMNE
Campus Nord UPC, 08034 Barcelona, Spain
ubach@cimne.upc.edu

Abstract

An evolved version of the rotation-free triangle shell element is presented. The advantages of this new element are threefold: simplicity, generality, and geometrical accuracy. The formulation is free from rotation degrees of freedom. The triangle here presented is independent from mesh topology, thus generality is conserved for any mesh-represented surface. Furthermore, the surface normal, and surface curvatures can be eventually computed for the reference configuration using the exact surface definition given by the CAD software.

The original approach is based on a low order interpolation of the basis functions. Computation of the curvatures is achieved by means of the construction of the gradient of the surface normal at each element. Since this is a non-conforming representation of the geometry, a higher order description of the geometry is needed. This is required to enrich the model and avoid local instabilities. Everything is achieved without introducing new degrees of freedom in the model.

The higher degree geometric description is based on the Bézier triangles concept, a very well known geometry in the domain of CAGD (Farin, Curves and Surfaces for CAGD, 2002). Using this concept we show the path to reconstruct a general third order interpolating surface using only the three coordinates at each node.

In all cases simplicity is of the utmost importance when dealing with boundary conditions. Boundary conditions are managed very easily, both for Dirichlet and Neumann conditions. The normal vector to the surface at every node accounts for this simplicity without the need to use additional degrees of freedom nor virtual nodes.

This work takes as starting point the nodal implementation of a basic triangle shell element (Oñate and Zárate, Rotation-free triangular plate and shell elements, 2000). In order to use an exact formula of the curvature, the normal directions at each node and the way to characterize them are proposed. Then, the geometrical properties and the mechanical behavior of the surface created are introduced. Finally, different examples are presented to depict the versatility and accuracy of the element.

1. Introduction

Several attempts have been made to overcome the C^1 condition that computing curvatures for shells demands. [1] [2] [3] [4] This work builds on the original proposal made by [5, 6] and extends those principles in order to gather richer geometrical information from the patch of all the elements —not only those sharing one side— surrounding a given triangle in the mesh. In doing this we can avoid the need for computing an averaged curvature for the element and instead we can obtain precise values for the curvature at any point in the triangle, in particular at the Gauss points.

The first time the current approach was introduced by Ubach and Oñate was in [7]. This early proposal was followed by the current framework also by Ubach and Oñate in [8]. However, it must be said that a work with the same principles was presented at the same congress by Linhard et al. [9].

2. Background

The original developments presented at the first congress does not lead to a satisfactory solution of the shell. The reason behind it is that zero energy modes affect the solution. Initially, we kept the geometric description of the element intentionally as simple as possible. As a consequence, it was possible for the mesh of triangles to fold like an accordion and not develop significant deformation energy; since because of the symmetry of the folds (see figure 1), the normals barely change direction making their gradient very close to zero. Thus the computed curvature using equation 1 results also negligible, even if the plane of the triangle differs a lot from the direction of the normals at the nodes.

$$\kappa = \nabla \underline{\boldsymbol{\varphi}} \cdot \nabla \underline{\boldsymbol{n}} \tag{1}$$

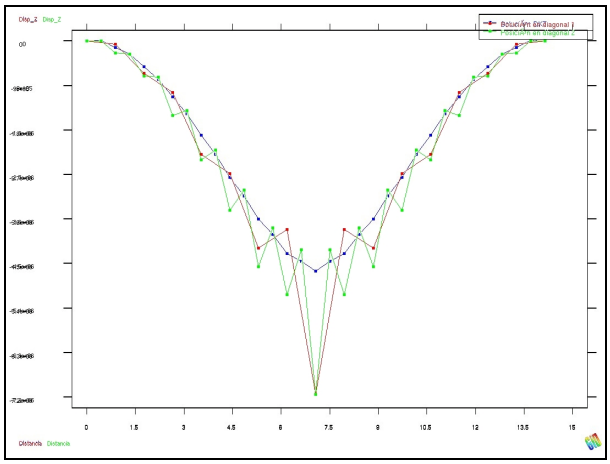

Figure 1: Numerical example showing the displacements along the diagonals (red and green) of a simply supported square with punctual load in the center. The results are shown compared to the corresponding solution given by the DKT element (blue).

We have explored different strategies to neutralize the instabilities caused by the lack of conformity in the description of the element:

- The simplest strategy consisted in making an analogy that assumed that the deviation of the normal from the theoretic perpendicular to the plane at the center of the element represented a rotation due to shear deformation.
- Another strategy consisted in assuming that the missing energy mode in the elements was an antimetric bending mode. Again, the deviation of the normal from the theoretic perpendicular at the center was used to estimate an increased deformation energy.
- Yet another strategy was devised. In this case the normal at the center of the element was prescribed to remain perpendicular to the element. To achieve this the triangle was further subdivided into three subtriangles.

In all cases the resulting finite elements were stable. However the strategies had as a secondary effect an increased stiffness of the shell, yielding smaller displacements than the theoretic ones.

3. Methodology

A different strategy consists on increasing the order of the description so that all the modes of deformation can be represented and thus avoiding the problems associated with the non-conforming formulation. The triangle of lowest order that can interpolate at the same time the positions and the normals at the nodes is a cubic triangle.

A way to disambiguate the parameters of the cubic triangle without increasing the number of degrees of freedom used is adopting the concept of Bézier triangles first defined by de Casteljau. [10, 11] See figure 2. All the equations deriving from this approach will be presented and discussed in detail.

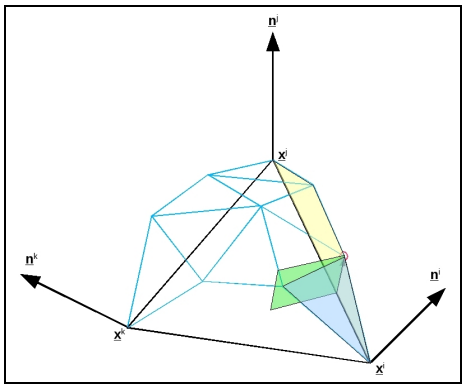

Figure 2: Representation of the net of control points for a cubic Bézier triangle using the nodal positions and the nodal normals to define the construction of each control point.

4. Results

The results are very satisfactory as will be shown in multiple examples. We advance here the convergence comparison for the classical roof shell problem between the present approach and the solution given by the DKT element.

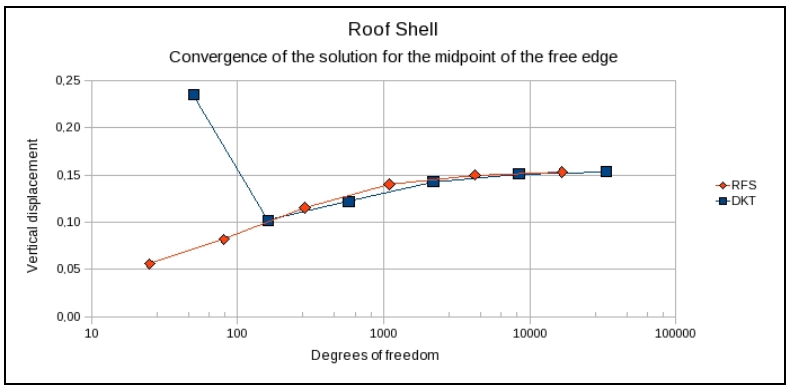

Figure 3: Comparison of the free edge midpoint's vertical displacement between the DKT element and the present RFS formulation and their convergences as the mesh is denser.

5. Conclusions

We present the development of a new rotation-free shell element. The only degrees of freedom used to solve the shells are the displacements of the nodes of the mesh. The approach is general and can be applied to any mesh topology. The results are very satisfactory.

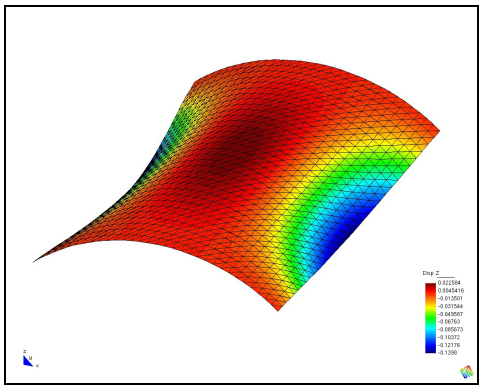

Figure 4: Picture showing a contour plot of the vertical displacements of the roof. The deformations have been scaled to magnify its appearance for better viewing.

On the numerical aspects of the present work, we note that by using only displacement degrees of freedom, we reduce considerably the size of the system matrix for any given mesh. The cost in return is an increase of the system matrix's bandwidth. The resulting bandwidth depends on the mesh topology, that is, the amount of elements surrounding any given node. For a regular triangular mesh (each node surrounded by 6 elements), the element's system matrix has 36 degrees of freedom.

References

[1] Oñate E. Cálculo de Estructuras por el Método de Elementos Finitos, 2nd Edition, CIMNE, 1995.

[2] Zienkiewicz O., Taylor R., El Método de los Elementos Finitos, 5th Edition, CIMNE, 2004.

[3] Cirak F., Ortiz M., Schröder P. Subdivision surfaces: a new paradigm for thin shell finite-element analysis. *International Journal for Numerical Methods in Engineering* 2000; 47 (12): 2039–2072.

[4] T. Hughes, J. Cottrell, Y. Bazilevs, Isogeometric analysis: Cad, Finite elements, NURBS, Exact geometry and mesh refinement. *Computer Methods in Applied Mechanics and Engineering* 2005; 194 (39-41): 4135–4195.

[5] Oñate E., Zárate F. Rotation-free triangular plate and shell elements. *International Journal for Numerical Methods in Engineering* 2000; 47: 557–603.

[6] Oñate E., Flores F. Advances in the formulation of the rotation-free basic shell triangle. *Computer Methods in Applied Mechanics and Engineering* 2005; 194 (21-24): 2406–2443.

[7] Ubach P.-A., Oñate E. New rotation-free composite shell triangle using accurate geometrical data. In *WCCM VII. 7th World Congress on Computational Mechanics*, Vol. CD-ROM, UCLA, iacm, Northwestern University, Los Angeles, California, USA, 2006.

[8] Ubach P.-A., Oñate E. Advances of the new rotation-free finite element shell triangle using accurate geometrical data. In *9th US National Congress on Computational Mechanics*, Vol. CD-ROM, University of California at Berkeley, USACM, San Francisco, California, USA, 2007.

[9] Linhard J., Bletzinger K.-U., Firl M. Upgrading membranes to shells - the ceg rotation free shell element and its applications. In *9th US National Congress on Computational Mechanics*, Vol. CD-ROM, University of California at Berkeley, USACM, San Francisco, California, USA, 2007.

[10] de Casteljau P. Outillages méthodes calcul, Tech. rep., A. Citroën, Paris (1959).

[11] Farin G. Curves and Surfaces for CAGD. A practical guide., 5th Edition, Morgan Kaufmann Publishers, 340 Pine Street, Sixth Floor, San Francisco, CA 94104-3205, USA, 2002.

Proceedings of the 6th International Conference on
Computation of Shell and Spatial Structures
IASS-IACM 2008: "Spanning Nano to Mega"
28-31 May 2008, Cornell University, Ithaca, NY, USA
John F. ABEL and J. Robert COOKE (eds.)

New curvature formulation of the SFE rotation-free shell element

Sylvain COUËDO*, Laëtitia DUIGOU* and Gérard RIO*

* Laboratoire d'Ingénierie des Matériaux de Bretagne, LIMATB, Université de Bretagne-Sud, UBS, Université Européenne de Bretagne, UEB
rue de Saint Maudé - BP92116, 56321 LORIENT CEDEX, FRANCE
couedo@univ-ubs.fr

Abstract

A new formulation for a family of thin shell finite elements is presented. The particularity of these shell finite elements is the rotation-free [3]. In order to improve these elements, a new formulation of curvature computation is developed. The results from classical linear benchmark examples are compared to study the differences between the new formulation and the former one, especially with unstructured meshes.

1 Convected Materials Coordinates, Kinematics of Shells

The element is formulated by using a convected material frame notion, which offers an interesting framework to take into account large transformations [3]. Classically, the position of point M is defined in a fixed cartesian frame $(O, \boldsymbol{I_a})$ (with $a = 1, 2, 3$) by its coordinates X^a : $\boldsymbol{OM} = X^a(M)\boldsymbol{I_a}$. Let us introduce a *convected curvilinear coordinates system* $\{\theta^i\}$. The midsurface is described by θ^3 ($-1 \leq \theta^3 \leq 1$), the thickness h is considered constant on all the midsurface. A point P of the midsurface is defined in *convected material framework* ($i = 1, 2$) by : $\boldsymbol{OP} = X^a(\theta^i)\boldsymbol{I_a}$. At each point P, a local frame vector can be defined :

$$\boldsymbol{a_\alpha} = \frac{\partial \boldsymbol{P}}{\partial \theta^\alpha} = \frac{\partial X^a}{\partial \theta^\alpha}\boldsymbol{I_a}, \text{ with } \alpha = 1, 2 \text{ ; and the normal } \boldsymbol{N} = \boldsymbol{a_3} = \frac{\boldsymbol{a_1} \wedge \boldsymbol{a_2}}{\|\boldsymbol{a_1} \wedge \boldsymbol{a_2}\|} \tag{1}$$

That leads to the midsurface metric tensor, defined by $\boldsymbol{A} = a_{\alpha\beta}\, \boldsymbol{a^\alpha} \otimes \boldsymbol{a^\beta}$ where $a_{\alpha\beta} = \boldsymbol{a_\alpha} \cdot \boldsymbol{a_\beta}$, and the curvature tensor (or second fundamental form) of the midsurface is $\boldsymbol{B} = b_{\alpha\beta}\, \boldsymbol{a^\alpha} \otimes \boldsymbol{a^\beta}$, where $b_{\alpha\beta} = \boldsymbol{a_{\alpha,\beta}} \cdot \boldsymbol{a_3} = -\boldsymbol{a_\alpha} \cdot \boldsymbol{a_{3,\beta}}$.

In our case, the θ^α material coordinates are the coordinates of the reference finite element. The local kinematics is obtained with the Kirchhoff hypothesis in finite transformations.

$$\boldsymbol{OM} = \boldsymbol{OP}(\theta^1, \theta^2) + \frac{\theta^3}{2} h \boldsymbol{N}(\theta^1, \theta^2) \tag{2}$$

The components of the Almansi strain tensor in finite transformations are :

$$\begin{aligned} \varepsilon_{\alpha\beta} \quad = \quad & \tfrac{1}{2}(\hat{a}_{\alpha\beta} - a_{\alpha\beta}) - \theta^3(\hat{h}\hat{b}_{\alpha\beta} - h b_{\alpha\beta}) \\ & + \tfrac{1}{2}(\theta^3)^2(\hat{h}^2 \hat{b}^\lambda_\alpha \hat{b}_{\lambda\beta} - h^2 b^\lambda_\alpha b_{\lambda\beta} + \hat{h}_{,\alpha}\hat{h}_{,\beta} - h_{,\alpha} h_{,\beta}) \end{aligned} \tag{3}$$

where the terms with "ˆ" refer to final time t and the terms without "ˆ" refer to the initial time $t = 0$. The strain tensor can be divided into two parts : the strain tensor of midsurface, or membrane strain tensor : $\frac{1}{2}(\hat{a}_{\alpha\beta} - a_{\alpha\beta})$ and the other terms, the flexion part, that depend of change of curvature tensor. This expression does not introduce any assumptions about small transformations. From the knowledge of the deformation, one can easily calculate strain rate (virtual or real) and stress for a particular behaviour, and finally to obtain the shell virtual power to include in the virtual principle. Hence, in this presentation, the key of the flexion model is the calculation of the curvature tensor.

The presented model is an amelioration of the SFE model [3], in which a base (finite) element is constituted by a central triangle with its three adjacent triangles. The curvature on the central triangle comes from a weighted averages of the central normal and the normals of the three frontier triangles.

The SFE element presents two originalities : the formulation in convected material coordinates and the reduced number of degrees of freedom (d.o.f.) per node (no degrees of freedom of rotation are needed). This reduces the computational time and large non-linear problems can be treated.

The principal limitation of the initial formulation is the sensitivity to mesh distortion. The accuracy for irregular meshes is unsatisfactory, only very regular meshes can lead to accurate results. So a new formulation, based on polynomial interpolation of the shape, is developed and compared with the former one. This polynomial description concerns the out of plane displacement (i.e. along the normal direction), expressed in the local frame. Using a second-degree polynomial interpolation of the six nodes, the position of a point M is defined by : $\theta^3(\boldsymbol{OM}) = a(\theta^1)^2 + b(\theta^2)^2 + c\theta^1\theta^2 + d\theta^1 + e\theta^2 + f$ where a, b, c, d, e, f are the unknowns.

2 Numerical results

The two formulations are tested on two classical linear benchmark examples and a geometrically non-linear problem.

2.1 Rhombic plate

A rhombic plate with two opposite sides simple supported and the other two sides free is subjected to a uniform load q. The results have been normalized with respect to the theoretical solution given by Razzaque [4]. This example has been investigated using two orientations and unstructured meshes (Fig. 1). The first two meshes on fig. 1 show respectively orientations A and B.

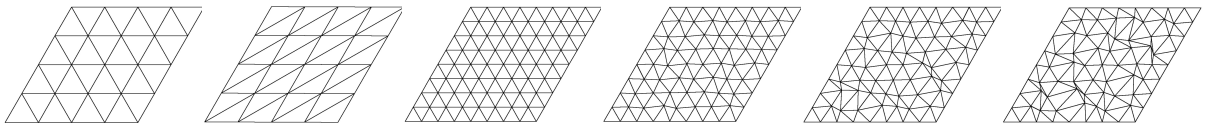

Figure 1: Rhombic Plate : Orientations (A) and (B) ; max. nodal perturbation from 0% to 30%

Mesh	BSQ [2]	S4 [1]	S3 (A) [5]	S3 (B) [5]	New SFE (A)	New SFE (B)
2x2	2,0559	2,1498	1,0381	1,0957	1,1490	1,2837
4x4	1,1851	1,2029	0,9821	0,9846	1,0272	1,0149
8x8	1,0248	1,0306	0,9746	0,9656	0,9992	0,9786
16x16	0,9987	1,0008	0,9810	0,9711	0,9942	0,9838
32x32	0,9946	0,9960	0,9876	0,9799	0,9941	0,9905

Table 1: Rhombic plate : Normalized central deflection for regular meshes

The interior grid points have been perturbed randomly. The maximum perturbations were chosen to be 0%, 10%, 20% and 30% of the distance between two adjacent grid points in the structured meshes (the last four meshes on fig. 1). The table 1 shows a good convergence for the new SFE element. One can note that New triangle SFE results have the same level of accuracy as quadrilateral elements(i.e. BSQ, S4 elements), but this New triangle SFE leads to a smaller bandwidth for the stiffness matrix. The table 2 shows a remarkable reduction of the sensitivity to the mesh distorsion.

Max. nodal perturb. (%)	Former SFE (A)	Former SFE (B)	New SFE (A)	New SFE (B)
0 (regular)	0,9744	0,9654	0,9992	0,9786
10	0.9662	0.94078	0.99816	0.977
20	0.9592	0.8792	1.0180	1.039
30	0.886	0.7629	1.030	1.0523

Table 2: Rhombic plate : Normalized central deflection (mesh 8x8)

2.2 Bending Patch Test

A classical bending patch test considers a square plate that is simply supported at three corners. A vertical load is applied at the free vertex. This allows to study behaviour of torsion.

The tables 3 and 4 show the vertical displacement of the point under the load with respect to the exact value. The regular meshes with orientation A and B give exactly the same numerical results, like the "S3" rotation-free shell [5]. The New SFE element gives good accuracy, like the rotation-free 4-node shells ([1] and [2]). The results show low sensitivity to nodal perturbation for the New SFE elements (meshes with 10x10 elements).

Mesh	1x1	2x2	4x4	8x8	16x16
S3 (A,B) [5]	0.349	0.554	0.662	0.854	0.921
New SFE (A,B)	0.9997	0.9977	0.9982	0.9987	0.9990

Table 3: Bending patch test : Normalized displacement

2.3 Cantilever beam subjected to end shear force

This example is a geometric nonlinear benchmark problem [6]. A cantilever beam clamped at one end is subjected to an end shear force P. A 16x1 mesh is used. The figure 2 shows very good agreement between the results. Note that these reference results are obtained by traditional shell elements, using d.o.f. of rotation.

3 Conclusion

In order to reduce the sensitivity to mesh distortion of SFE rotation-free shell finite element, a new formulation based on polynomial interpolation is studied.

The results from linear benchmark examples and non-linear problem are very precise. Compared with the former formulation of SFE, the sensitivity to the deformation of the mesh is notably decreased, at the point it becomes negligible.

References

[1] M. Brunet, F. Sabourin. *Analysis of a rotation-free 4-node shell element* Int. J. Num. Meth. Engng., 66, pp 1483-1510, 2006

Max. nodal perturbation	0% (regular)	10%	20%	30%
Former SFE	0.879	0.869	0.826	0.756
New SFE	0.9990	0.9992	1.003	1.026

Table 4: Bending patch test : Normalized displacement and nodal perturbation (mesh 10x10)

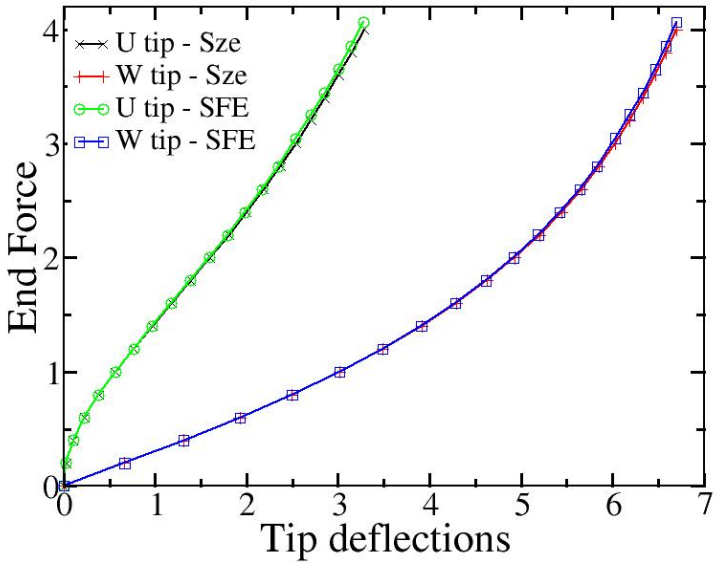

Figure 2: Load-deflection curves for cantilever beam subjected to end shear force

[2] F.G. Flores, C.F Estrada *A rotation-free thin shell quadrilateral* Comput. Methods Appl. Mech. Engrg., 196, pp 2631-2646, 2007

[3] H. Laurent, G. Rio. *Formulation of a thin shell finite element with C^0 and convected material frame notion* Computational Mechanics, 27, pp 218-232, 2001

[4] A. Razzaque. *Program for triangular bending element with derivative smoothing* Int. J. Numer. Meth. Engng., 6, pp 333-343, 1973

[5] F. Sabourin, M. Brunet. *Detailed formulation of the rotation-free triangular element "S3" for general purpose shell analysis* Engineering Computations, 23, pp 469-502, 2006

[6] K.Y. Sze, X.H. Liu, S.H. Lo. *Popular benchmark problems for geometric nonlinear analysis of shells* Finite Element in Analysis and Design, 40, pp 1151-1569, 2004

Proceedings of the 6th International Conference on
Computation of Shell and Spatial Structures
IASS-IACM 2008: "Spanning Nano to Mega"
28-31 May 2008, Cornell University, Ithaca, NY, USA
John F. ABEL and J. Robert COOKE (eds.)

Largest geometrically exact nonlinear thin beam, plate & shell elements and c-type FEM

Debabrata RAY*

*Institute for Dynamic Response, Inc.
32 North Hill Court, Oakland, CA 94618, USA
Dr.Ray@DrUnSTRESS.com

Abstract

A method, denoted as **c-type** has been applied by constructively defining a finite element space by Bezier (and de Boor) control vectors as the generalized displacements and the Bernstein polynomials (and B-Splines) as the elemental basis functions. In this context, geometrically exact nonlinear, curved beam, plate and shell element formulations are presented for iso/subparametric finite element analysis with the symmetric geometric stiffness matrix expressed in its most simple, direct and explicit form compared to those available in the published literature. The goal of solving problems ranging from tortuous curved beams to plates and shells modeled as a truly three-dimensional element with extreme non-linearity by a minimal number of 'mega' elements compared to the 'standard' finite elements in the literature has been successfully constructed with no shear locking.

1. c-Type Method

A discussion of c-type method has been presented in a previous paper [1]. In summary, for Finite Element Analysis (FEA) of the 'mega-size', arbitrary shaped elements delivered as the outcome of a Computer-Aided Mesh Generation (CAMG) scheme, the method is based on geometrically constructed Bezier-Bernstein-deBoor polynomial finite element space with local support and devoid of adhocisms such as under-integration or any of the pitfalls, namely, shear-locking, etc., associated with the conventional finite element methods.

2. Geometrically Nonlinear Formulation

Starting with Reissner [2], all noteworthy works that followed presented formulations with the geometric stiffness tensor either in a differential operator form as in [3] or in an approximate form as in [4]; an exact and explicit expression is necessary for the 'mega' curved element formulation; a central lemma, missing in the literature, provides for the closed form expressions and the associated exact geometric stiffness tensor for beams. Similar result is obtained for arc lengths S_1 and S_2 along the lines of curvature of a shell; in fact, considering a shell surface as the confluence of beams along its lines of curvatures, all shell equations are adapted in a unified way from the corresponding beam formulation.

2.1 Nonlinear finite element formulation

For simplicity and without loss of much generalization, we restrict ourselves to only static equilibrium equations of deformed states in terms of parameters measured in undeformed curvilinear coordinate system; the beam kinematic is completely described by $(\mathbf{d}, \mathbf{R})$ with $\mathbf{d}$, the displacement vector field, and, $\mathbf{R}$, as the rotational tensor field parameterized by $\boldsymbol{\theta}$, the Rodrigues vector field. With the augmentation of relevant pairs such as $\hat{\mathbf{d}} = \{\mathbf{d} \quad \tilde{\quad}\}^T$, etc., the generalized nodal vector describing the deformation of a three-dimensional curved

beam, let $\mathbf{q}^d$, $\overline{\mathbf{q}}^d$ and $\Delta\mathbf{q}^d$ be the displacement, virtual and incremental Bezier control vectors. The augmented generalized incremental strain-displacement control matrix:

$$\mathbf{E}(\hat{\mathbf{d}}) = \begin{bmatrix} \mathbf{R}^{\mathrm{T}} & \mathbf{0} \\ \mathbf{0} & \mathbf{R}^{\mathrm{T}} \end{bmatrix} \begin{bmatrix} [\mathbf{k}^0] & [\mathbf{a}]\mathbf{W} & \mathbf{I} & \mathbf{0} \\ \mathbf{0} & \mathbf{X}+[\mathbf{k}^c]\mathbf{W} & \mathbf{0} & \mathbf{W} \end{bmatrix} \tag{1}$$

with $\mathbf{a} \equiv \mathbf{e} + \mathbf{k}^0 \times \mathbf{d}$, $\mathbf{k}^0 = \begin{pmatrix} \tau & 0 & k \end{pmatrix}^{\mathrm{T}}$ is the undeformed curvature vector, $\mathbf{e} \equiv \hat{\mathbf{1}} + \mathbf{d}^t{}_{,s}$ with $\hat{\mathbf{1}} \equiv \begin{pmatrix} 1 & 0 & 0 \end{pmatrix}$, the unit vector, and $[\mathbf{k}^c] \equiv [\mathbf{k}^0] + [\mathbf{k}^t]$, the total current "curvature" skew matrix; $\mathbf{G}$ is composed of symmetric (in the absence of distributed moment loading) sub-matrices given as:

$$\begin{aligned}
\mathbf{G}_{12} &\equiv [\mathbf{k}^0][\mathbf{F}^t]\mathbf{W} \\
\mathbf{G}_{22} &\equiv \tfrac{1}{2}\mathbf{W}^{\mathrm{T}}\{[\mathbf{F}^t \otimes \mathbf{a}] + [\mathbf{a} \otimes \mathbf{F}^t] - 2(\mathbf{F}^t \bullet \mathbf{a})\}\mathbf{W} + c_2(\ \bullet\ ^f) \\
&\quad + \tfrac{1}{2}([\mathbf{h}^b \otimes\ ] + [\ \otimes\ ^b]) \\
&\quad + \tfrac{1}{2}\mathbf{W}^{\mathrm{T}}\{[\mathbf{M}^t \otimes \mathbf{k}^c] + [\mathbf{k}^c \otimes \mathbf{M}^t] - 2(\mathbf{M}^t \bullet \mathbf{k}^c)\}\mathbf{W} + c_2(\ \bullet\ ^m) \\
&\quad + \tfrac{1}{2}([\mathbf{h}^m \otimes\ ] + [\ \otimes\ ^m]) + \ ^{\mathrm{T}}[\ ^t] + [\ ^t]^{\mathrm{T}} \\
\mathbf{G}_{23} &\equiv \mathbf{W}^{\mathrm{T}}[\mathbf{F}^t] \\
\mathbf{G}_{24} &\equiv \mathbf{W}^{\mathrm{T}}[\mathbf{M}^t]\mathbf{W} + \mathbf{Y}(\mathbf{M}^t)
\end{aligned} \tag{2}$$

and $\hat{\mathbf{D}}^n \equiv diag\{EA \quad GA_m \quad GA_b \quad GJ \quad GI_m \quad GI_b\}$ is the constitutive matrix..

Similar results, as in the case of a beam presented above, exist for shells except for the fact that we have two arc length parametrizations along the lines of curvatures of the shell. Thus, the tangesnt stiffness now has two additive parts due to two dimensions of the shell surface each similar to what has already been presented above for the beam

3. Numerical Examples

3.1 Example 1: A frequently referred 2D planar curved frame with out-of-plane tip load is considered with deformed shape at various load level shown in figure 1 and tip deformation in the adjoining table.

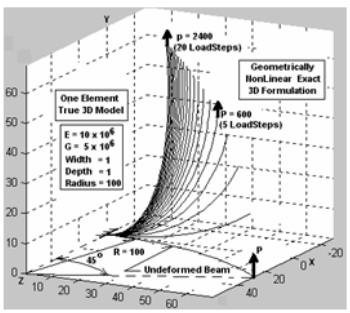

(a)

Beam Model	Load Level & tip deformed location						No. Of Elems Needed
	300			600			
	x	y	z	x	y	z	
c-Type	22.24	58.78	40.20	15.69	47.15	53.48	1
Simo & Vu-Quoc,[3]	22.33	58.84	40.08	15.79	47.23	53.37	8
Cardona & Geradin,[4]	22.14	58.64	40.35	15.55	47.04	53.50	8
Bathe&Bolourchi,[5]	22.5	59.2	39.5	15.9	47.2	53.40	8

(b)

Figure 1: (a) Model definition and deformations at different load level, (b) element comparisons

It took only a ***single*** "mega" element with full Gauss integration and without any shear locking , five load steps to arrive at a load level of 600 compared to sixty equal load steps, [14]. A comparison of deformed tip positions for reported load levels are shown in Table 1. It took.

3.2 Example 2: The robustness of the **c-type** method is tested where the beam is modeled by two truly three - dimensional elements as shown in figure 2(a). The deformed shapes are shown in figure 2(c)

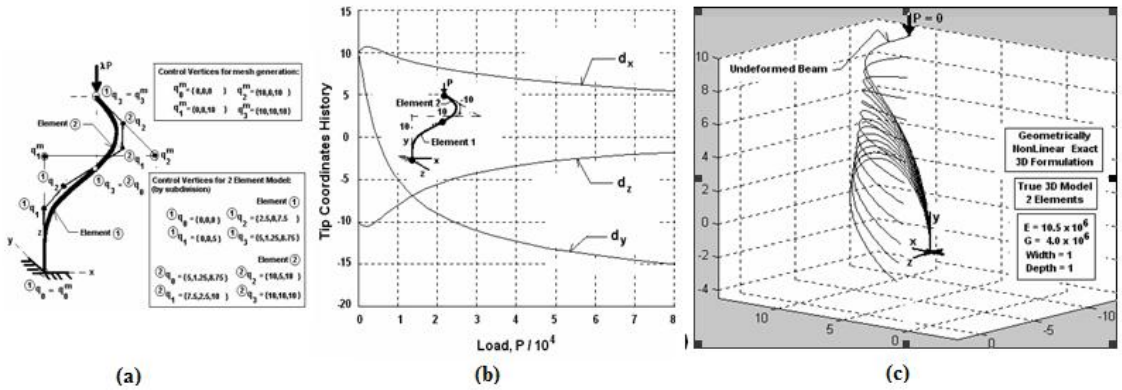

Figure 2: (a).the true 3D Model definitions, (b) coordinate history, (c) deformed shapes

It may be pointed out that it takes more than one order of higher numbers of currently available elements than ***two*** 'mega' c-type elements utilized here to match the presented accuracy, Taylor & Ray [6]..

3.3 Example 3: This is the familiar shell example known as "Scordelis-lo-roof" in the literature. The deflected shapes with quintessential "kick-in" behavior and the load-deformation curve of one quadrant of a shell modeled by a ***single*** c-type element are shown in Figure 3(a) and 3(b).

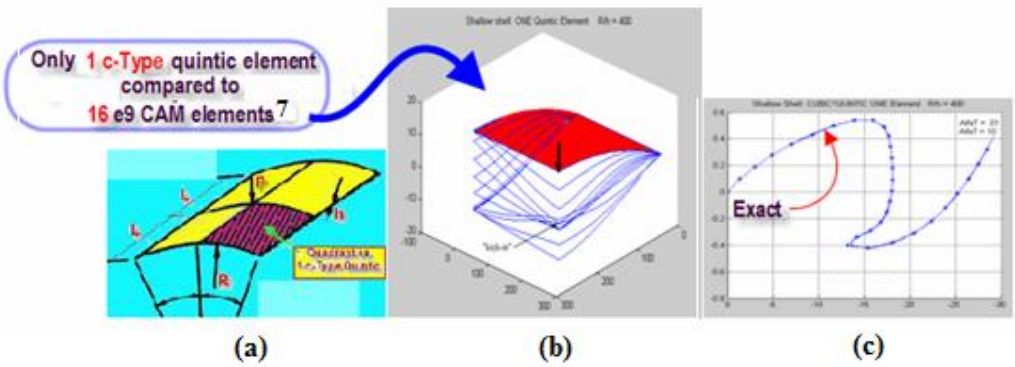

Figure 3. (a) model, (b) the deflected shapes, (b) load-deformation at the center of "Scordelis lo-roof".

3.4 Example 4: This is the familiar hemispherical shell with apical hole undergoing nearly inextensional bending deformations under two inward and two outward opposing forces. The linear solution is obtained with ***one*** element; the nonlinear response to 70% of the initial radius is accurately recovered with $3x3$ mesh of elements for a quadrant. The model, deformed shape and the load=deformation , and, the comparison of numerical effciency in terms of the 'mega' character of the c-type elements, is indicated in figure 4.

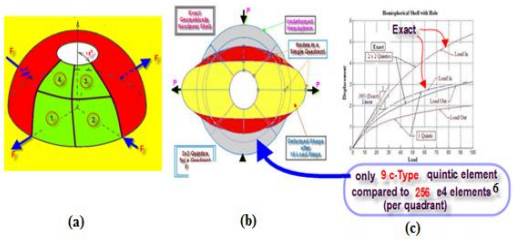

Methods	Number of elements with comparable accuracy	
c-type FEM	4 quintics	9 quintics
Simo, et al [8]	64 elements	256 elements
Chroscielewski, et al [7]	64 elements	256 elements

Figure 4. (a) problem, (b) deformed shape, (c) load-deformation at load points, and, (d) element comparison: 'mega' character of the c-type elements

4. Conclusions

The robustness, accuracy and numerical efficiency of the ***c-type 'mega' elements*** are self-evident from examples presented in the paper. As a geometrically constructed B-spline finite element space, the **c-type** method subsumes familiar spaces such as Lagrange, Hermite, etc. and conventional **h**- and **p**-type methodologies both conceptually and computationally. Accordingly, the practiced, general-purpose computer programs currently in use can be readily adapted to produce 'crime-free' (in the sense of Strang and Fix [9]), convergent, controlled and cost-efficient procedure that unifies modeling and analysis.

References

[1] Ray D. c-Type method of unified CAMG & FEA. Part I: Beam and arch mega-elements—3D linear and 2D non-linear. *International Journal for Numerical Methods in Engineering*. 2003, **58**:1297--1320

[2] Reissner E. On one-dimensional large displacement finite strain beam theory. *Studies Appl. Math.* 1973; **52**:67-95.

[3] Simo JC, Vu-Quoc L. A three-dimensional finite strain rod model. Part II: Computational Aspects. *Computer Methods in Applied Mechanics and Engineering* 1986; **58**(1):79-116.

[4] Cardona A, Geradin M. A beam finite element non-linear theory with finite rotations.. *International Journal for Numerical Methods in Engineering* 1988; **26**:2403-2438.

[5] Bathe KJ, Bolourchi S. Large displacement analysis of three-dimensional beam structures. *International Journal for Numerical Methods in Engineering* 1979; **14**: 961-986.

[6] Taylor RL, Ray D. Rods – some developments for large displacements. 5th International Conference on Computation of Shell and Spatial Structures. 2005, Austria.

[7] Chroscielewski J, Makowski J, Stumpf H. Finite element analysis of smooth, folded and multi-shell structures. *Computer Methods in Applied Mechanics and Engineering* 1997: **141**:1-46.

[8] Simo JC, Fox DD, Rifai MS. On a stress resultant geometrically exactshell model. Part III: Computational aspects of the nonlinear theory. *Computer Methods in Applied Mechanics and Engineering* 1990: **79**:21-70.

[9] Strang G, Fix G. An Analysis of the Finite Element Method, Prentice Hall, 1973

Proceedings of the 6th International Conference on
Computation of Shell and Spatial Structures
IASS-IACM 2008: "Spanning Nano to Mega"
28-31 May 2008, Cornell University, Ithaca, NY, USA
John F. ABEL and J. Robert COOKE (eds.)

A new shell element for elasto-plastic finite strain analysis. Application to the collapse and post-collapse analysis of marine pipelines

Rita TOSCANO * and Eduardo DVORKIN
SIM&TEC
Av. Pueyrredón 2130
C1119ACR Buenos Aires, Argentina
rtoscano@simytec.com

Abstract

The infinitesimal strain version of the MITC4 shell element (Dvorkin and Bathe [6]) was previously successfully used for the analysis of deep-water applications of steel marine pipelines. The collapse and post collapse responses were modeled and compared with experimental results (Toscano et al. [12]). Even though in those verifications the matching between numerical and experimental results was excellent, it was also noticed that in the post–collapse regime very high strains are developed in the steel shell. In Ref. [12] a version of the MITC4 that uses a posteriori updates of the shell thickness was used to incorporate into the model the finite strain behavior. The results indicated that even though the consideration of finite strains improves the solution, the room for improvement - when the overall equilibrium paths are considered - is so small that it hardly justifies the use of a more expensive numerical model. However, if local strains are sought, the finite strain model produces much better approximations to the actual situation. Hence, the motivation for shell element formulations apt for finite strain elasto-plastic analyses is still opened.

In previous publications we presented a new shell element formulation, the MITC4-3D that we developed for finite strain analysis (Toscano and Dvorkin [13, 14]) using the MITC4 strains interpolation (Dvorkin and Bathe [6]) and 3D constitutive relations.

In this paper we are going to discuss the basic features of the MITC4-3D element and present further verification / validation.

1. Introduction

In 1970, Ahmad, Irons and Zienkiewicz [1] presented a shell element formulation that after many years still constitutes the basis for modern finite element analysis of shell structures. Even tough the A-I-Z shell element was a breakthrough in the field of finite element analysis of shell structures, under the constraint of the infinitesimal strains, it suffers from the locking phenomenon and much research effort has been devoted to the development of A-I-Z type elements that do not present this problem (Bathe [2], Chapelle and Bathe [3], Zienkiewicz and Taylor [15],).

The MITC4 shell element (Dvorkin and Bathe [6]), which was developed to overcome the locking problem of the A-I-Z shell elements has become, since its development in the early eighties, the standard shell element for many finite element codes. However, the limitation of infinitesimal strains is still present in the MITC4 formulation.

In 1995 Dvorkin, Pantuso and Repetto [7] developed the MITC4-TLH element, that based on the original MITC4 formulation can model finite strain elasto-plastic deformations. This element imposes the condition of zero transversal stresses and its computational cost is rather high.

In the present paper we present an element that is also based on the MITC4 formulation and can efficiently model finite strain deformations using a general 3D elasto-plastic material model.

The most relevant differences with the original MITC4 formulation are:

- For each quadrilateral element we have 22 d.o.f.: 5 generalized displacements per node plus 2 extra d.o.f. to incorporate the through-the-thickness stretching.
- We use a general 3D constitutive relation instead of the original laminae plane stress constitutive relation.

2. The MITC4-3D formulation

Some of the basic features of our MITC4-3D element are:

- The shell geometry is interpolated using mid-surface nodes and director vectors.
- The nodal displacements and transverse shear strains are interpolated using the original MITC4 formulation (Dvorkin and Bathe [6]).
- For interpolating the director vectors special care is taken to avoid spurious director vector stretches (Gebhardt and Schweizerhof [8], Simo *et al*. [9-11]).
- Two additional degrees of freedom are considered to include a linear thickness stretching. These thickness-stretching degrees of freedom are condensed at the element level.

2.1 Shell element geometry

Following the MITC4 formulation we define, in the reference configuration, nodes on the shell mid-surface and at each node we define a director vector which represents, at that node, an approximation to the shell mid-surface (Dvorkin and Bathe [6], Simo *et al*. [9-11]).

Therefore, defining inside the element the natural coordinate system (r,s,t) (Bathe [2]), for an element with constant thickness, we can write,

$$ {}^{\tau}\underline{x}(r,s,t) = h_k(r,s)\cdot {}^{\tau}\underline{x}_k + \frac{t}{2}\cdot\left({}^{\tau}\lambda_0 + {}^{\tau}\lambda_1\cdot t\right)\cdot\frac{h_k(r,s)\cdot {}^{\tau}\underline{V}_n^k}{\left\| h_k(r,s)\cdot {}^{\tau}\underline{V}_n^k \right\|}\cdot a \qquad (1) $$

Where,

$h_k(r,s)$: isoparametric 2D interpolation functions (Bathe [2]),

${}^{\tau}\underline{x}$: k-node position vector,

a : constant element thickness,

${}^{\tau}\underline{V}_n^k$: k-node director vetor; with $\left\| {}^{\tau}\underline{V}_n^k \right\| = 1.$

In Eqn. (1) ${}^{\tau}\lambda_0$ is a constant thickness stretching and ${}^{\tau}\lambda_1$ is the through-the-thickness stretching gradient. In our formulation the element ${}^{\tau}\lambda_0$ and ${}^{\tau}\lambda_1$ are discontinuous across element boundaries and they will be condensed at the element level.

2.2 Incremental displacements

The incremental displacements to evolve from the τ-configuration to the τ+Δτ-configuration are,

$$ \underline{u}(r,s,t) = h_k(r,s)\cdot\underline{u}_k + \frac{t}{2}\cdot\left({}^{\tau}\lambda_0 + \Delta\lambda_0 + {}^{\tau}\lambda_1\cdot t + \Delta\lambda_1\cdot t\right)\cdot\frac{h_k(r,s)\cdot {}^{\tau+\Delta\tau}\underline{V}_n^k}{\left\| h_k(r,s)\cdot {}^{\tau+\Delta\tau}\underline{V}_n^k \right\|}\cdot a \qquad (2) $$

For the director vector rotations we can write,

$$ {}^{\tau+\Delta\tau}\underline{V}_n^k = {}^{\tau+\Delta\tau}_{\tau}\underline{\underline{R}}\cdot {}^{\tau}\underline{V}_n^k $$

where ${}^{\tau+\Delta\tau}_{\tau}\underline{\underline{R}}$ is a rotation tensor (Dvorkin *et al*. [5]).

To simplify the formulation, we made the approximation $\left\| h_k(r,s)\cdot {}^{\tau+\Delta\tau}\underline{V}_n^k \right\| = \left\| h_k(r,s)\cdot {}^{\tau}\underline{V}_n^k \right\|$

2.3 Constitutive relation

The shell element formulation developed in this paper is a fully 3D formulation since the in-layer plane stress hypothesis used in the original MITC4 formulation was not invoked in this case. This full 3D constitutive relation is based on:

- Lee´s multiplicative decomposition of the deformation gradient (Figure 1)
- Maximum plastic dissipation
- For the elastic part an hyperelastic relation using Hooke with Hencky strains: ${}^{\tau}_{0}\underline{\underline{\Gamma}} = \underline{\underline{\underline{\underline{C}}}} \cdot {}^{\tau}_{0}H$.

${}^{\tau}_{0}\Gamma^{IJ}$ are calculated as the rotational pull-back of the contravarian components of the Kirchhoff stress tensor. For an ***isotropic*** material, the second order tensor ${}^{\tau}_{0}\underline{\underline{\Gamma}}$ is the stress measure energy-conjugate to the Hencky strain tensor (Dvorkin and Goldschmit [7]).

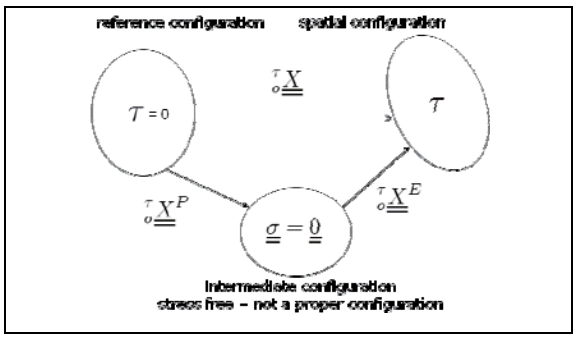

Figure 1: Lee's multiplicative decomposition

3. The incremental formulation

Using a total Lagrangian formulation we can write the Principle of Virtual Work for the equilibrium configuration at τ+Δτ (Bathe [2]),

$$\int_{{}^{0}V} {}^{t+\Delta\tau}\underline{\underline{\Gamma}} : \delta\underline{\underline{H}}^{E} \cdot {}^{0}dV = {}^{t+\Delta\tau}\underline{\Re}$$

where ${}^{t+\Delta\tau}\underline{\Re}$ is the virtual work of the external loads acting on the solid body in the τ+Δτ-configuration and $\underline{\underline{H}}^{E}$ is an elastic Hencky strain tensor.

The resulting stiffness matrices are, of course, symmetric.

4. Numerical results

4.1 Infinitely long cylinder under internal pressure

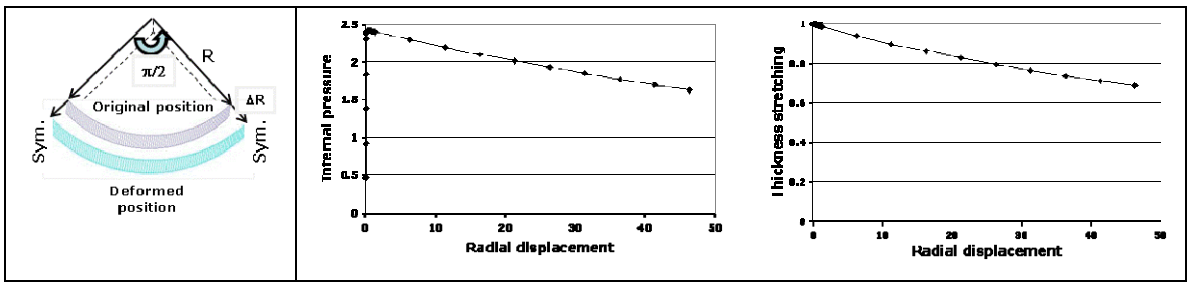

Figure 2: Inflation of an Infinitely long elasto-plastic cylinder

We consider the infinite cylinder represented in Fig. 2 under internal pressure (R_{int}=100. , E=2.1 10^6, E_t=2.1 10^3, a=0.1, μ=0.3, σ_y=2.1 10^3). In the same figure we represent the equilibrium paths obtained for the infinitely long cylinder as well as the predictions of the through-the-thickness stretching.

The d.o.f. ($\Delta\lambda_0$, $\Delta\lambda_1$) are condensed at the element level and (20x20) element stiffness matrices are obtained and assembled into the global stiffness matrices.

4. Conclusions

On the basis of the MITC4 shell element formulation, we developed the MITC4-3D shell element formulation for finite strain analyses of shell structures using general 3D constitutive models. In this paper the new element was implemented for the analyses of elasto-plastic shell structures and the results indicate that it is a very effective element.

5. References

1. Ahmad S, Irons B.M. and Zienkiewicz O.C. (1970), "Analysis of thick and thin shell structures by curved finite elements", Int. J. Numerical Methods in Engng., vol. 2, pp.419-451.
2. Bathe K.J. (1996), Finite Element Procedures, Prentice Hall, Upper Saddle River,NJ.
3. Chapelle D. and Bathe K.J. (2003), The Finite Element Analysis of Shells - Fundamentals, Springer, Berlin.
4. Dvorkin E.N., Pantuso D. and Repetto E.A. (1995), "A formulation of the MITC4 shell element for finite strain elasto-plastic analysis", Comput. Meth. Appl. Mechs. Engng., vol. 125, pp.17-40.
5. Dvorkin E.N., Oñate E. and Oliver J. (1988), "On a nonlinear formulation for curved Timoshenko beam elements considering large displacement/rotation increments", Int. J. Numerical Methods in Engng., vol. 26, pp. 1597-1613.
6. Dvorkin E.N. and Bathe K.J., "A continuum mechanics based four-node shell element for general nonlinear analysis", Engng. Computations, Vol. 1, pp. 77-88, 1984.
7. Dvorkin E.N. and Goldschmit M.B. (2005), Nonlinear Continua, Springer, Berlin.
8. Gebhardt H. and Schweizerhof K. (1993), "Interpolation of curved shell geometries by low order finite elements - Errors and modifications", Int. J. Numerical Methods in Engng., vol. 36, pp.287-302.
9. Simo J.C. , Fox D.D. and Rifai M.S. (1989), "On a stress resultant geometrically exact shell model. Part II: The linear theory; computational aspects", Comput. Meth. Appl. Mechs. Engng., vol. 73, pp.53-92.
10. Simo J.C., Fox D.D. and Rifai M.S. (1990), "On a stress resultant geometrically exact shell model. Part III: Computational aspects of the nonlinear theory", Comput. Meth. Appl. Mechs. Engng., vol. 79, pp.21-70.
11. Simo J.C., Fox D.D. ans Rifai M.S. (1992), "On a stress resultant geometrically exact shell model. Part IV: Variable thickness shells with through-the-thickness stretching", Comput. Meth. Appl. Mechs. Engng., vol. 81, pp.91-126.
12. Toscano R.G., Mantovano L., Amenta P., Charreau R., Johnson D., Assanelli A. and Dvorkin E.N., "Colapse arrestors for deepwater pipelines. Cross-over mechanisms", Computers&Structures 86 (2008) 728-743.
13. Toscano R.G. and Dvorkin E.N., "A shell element for elasto – plastic finite strain analyzes", Proceedings 9th US National Congress on Computational Mechanics, Offshore Technology Conference, San Francisco, USA, July 2007.
14. Toscano R.G. and Dvorkin E.N., "A Shell Element for Finite Strain Analyses. Hyperelastic Material Models", Engineering Computations, Vol.24, N° 5, pp.514-535, 2007.
15. Zienkiewicz O.C. and Taylor R.L. (2000), The Finite Element Method, Vol. 2, 5th Edition, Butterworth-Heinemann.

Proceedings of the 6th International Conference on
Computation of Shell and Spatial Structures
IASS-IACM 2008: "Spanning Nano to Mega"
28-31 May 2008, Cornell University, Ithaca, NY, USA
John F. ABEL and J. Robert COOKE (eds.)

A finite element analysis of axially crushed corrugated frusta

Mahmoud M. A. YOUNES

Lecturer, department of engineering mechanics, M.T.C., Cairo, EGYPT.
myounes27@yahoo.com

Abstract
Failure analysis of corrugated shells requires knowledge of the behavior of a shell structure as it is crushed. Investigation of this problem is presented in this paper. The axial crushing of a right circular axi-symmetric corrugated frusta subjected to quasi-static compression is numerically studied. The finite element code ABAQUS/Explicit was employed to predict the crushing behaviour and the effect of different geometric parameters required to enhance the energy absorption capability of corrugated frusta. The main objectives are to establish the load-deflection response of the axi-symmetric corrugated frusta and to describe the overall deformation of the frusta, since this data greatly affect the energy absorbed by frustum models. The present simulation also provides a simple demonstration of the capabilities of ABAQUS/Explicit for modeling contact problems between deformable bodies and rigid, impenetrable surfaces. Results showed that as the number of corrugations along a frustum generator increases, the amount of absorbed energy significantly increases, however the collapse modes of those corrugated frusta are qualitatively similar. The influence of varying the axial length-to-thickness ratio and the corrugation angle on the crashworthiness performance of frustum models are predicted and the obtained finite element results are depicted.

Keywords: Finite element; Corrugated frusta; Axial loading; Energy absorption; Collapse

1. Introduction
Frusta (truncated circular cones) have wide ranges of applications among the most efficient energy absorption structural members [1]. Mamalis et al. [2-4] reported experimental results of axial crushing of aluminum and steel cylinders and frusta and an expression has been introduced for the crushing load by fitting the experimental results corresponding to axi-symmetric and diamond failure modes. Mamalis et al. [5-6] used kinematics to study the collapse mechanism in PVC tubes and frusta subjected to axial load. El-Sobky and Singace [7] examined experimentally the stress distribution of elastically loaded frusta subjected to axial loading. The energy absorption characteristics and the collapse modes of axially crushed frusta of different geometric ratios and end-constraints were depicted quasi-statically [8] and dynamically [9].
This paper explores the crushing behaviour of corrugated frusta by using the commercially available finite element code ABAQUS/Explicit version 6.4 [10]. The main objectives are to predict the collapse mechanism of the axially crushed corrugated frusta and to examine the main different parameters affecting the energy absorption capability.

2. Finite element model
ABAQUS version 6.4 was used to predict the behaviour of the axially crushed corrugated frusta. Throughout the simulation process, three different geometries of frusta have been modeled, which are straight frustum, corrugated frusta with different corrugation angles ($\alpha=5^{\circ}$: $\alpha=45^{\circ}$) and a frustum with higher number of corrugation surfaces. Moreover, different axial length-to-thickness ratio (L/t=53 : L/t=243) were used in modeling corrugated frusta. In order to verify the finite element model, the global dimensions of the corrugated frusta used in ABAQUS were essentially identical to that of the straight frustum specimens tested by El-Sobky et al. [8]. All the frusta used in the finite element simulation were constraints free with 51.6 mm top mean

diameter, 151.6 mm base mean diameter and 133.7 mm axial length. The shell element S4R was used in the modelling. The element S4R is a three-dimensional, doubly curved, four-node shell element. Each node has three displacement and three rotation degrees of freedom. This element is considered a general purpose shell element because it is valid for use with both thin and thick shell problems and it allows for large strains as load increases.

3. Validation of the finite element model

In order to insure the finite element model was sufficiently accurate, it was validated using the experimental results in Ref.[8] which depicted the gradual propagation of the collapse mechanism for an axially crushed straight frustum under quasi-static compressive loading. Any discrepancy appeared in Fig.(1) may be attributed to the presence of imperfections in the frustum test specimens and the variation in thickness along the meridian direction of the spun frusta. These imperfections were produced from the spinning process used in manufacturing of the frustum specimens.

4. Collapse mechanisms

4.1. Straight frusta

It is noted that the collapse of the crushed straight frustum model is initiated with the formation of an inward inverted axi-symmetric ring at the top of the frustum end as seen in Fig.(2). This inversion is accompanied by an initial peak load observed in the load-displacement curve. Progressive compression enforces the edge of the base to move radially outwards (away from the axis of frustum) and an axi-symmetric plastic hinge is formed at the contact with the lower rigid surface.

4.2. Corrugated frusta

Apart from the straight frusta, Fig.(3) reveal that failure mechanisms of corrugated frusta show different characteristics. Two finite element frusta of different corrugation numbers (5 and 25) are modeled to investigate the failure mechanisms.

In the initial stage of compression, the frustum model behaves as if its ends are fixed because of the influence of friction between the model edges and the rigid surfaces. Furthermore, the base of the model starts to be flattening on the lower rigid surface. Increasing the compression generates a plastic bending hinge in only one corrugation at the top of the model. Formation of the plastic hinge produces a single axi-symmetric fold at the highest corrugation which is moving with the displacement of the upper plate. During the folding of the first corrugation, the second adjacent corrugation below the first one begins slightly to be folded in the same previous manner. Folding of the second corrugation was totally carried out after the upper pate has traveled and became in contact with the current corrugation and directly pushed it downward. Progressive compression reveals that, all corrugations are folded gradually in the same manner and the frustum models are collapsed in axi-symmetric accordion modes independent of the number of corrugations.

5. The load- and energy-displacement curves

The load-displacement curves and the corresponding absorbed energy for a straight and corrugated frusta with different number of corrugations are shown in Fig.(4). In practice this load is very important from the design point of view because it gives an indication of the force required to initiate collapse & hence begin the energy absorption process. Moreover, the straight frustum model reflects highly non-uniform characteristics and overshoots in the load-displacement curve.

The load-displacement curve in Fig.(4) of corrugated frusta with 5 corrugations shows highly stable and uniform characteristics where the fluctuations, peaks and valleys are repeated in a regular manner. Each peak represents the localized collapse force initiated during the folding of each corrugation. Generally, the load rises steeply with upper and lower boundaries. The slope of the upper load boundary is greater than the slope of the lower load boundary in the curve of the 25 corrugations model and vice versa in the curve of the 5 corrugations model.

6. Effect of the number of corrugations

Regular corrugations are a condition in all simulations curried out in this paper. The deformation mechanism and the energy absorption capacity of the corrugated frustum with 5 corrugations are compared with that of the 25 corrugations. It was found that, the two corrugated frusta of 5 and 25 corrugations are crushed in a similar regular manner with axi-symmetric accordion failure modes as shown in Fig.(3). However, the number of corrugations factor was found to have a significant role in the frustum energy absorption capacity. Hence, the

deformation shape of a corrugated frustum is independent on the number of corrugations, while increasing the number of corrugations increases the capability of the frustum to absorb energy.

7. Effect of the corrugation angle α

The variation of the absorbed energy of the corrugated frusta with different corrugation angles ranged from 0° to 45° is shown in Fig.(5). This figure may be divided into three zones in order to have the ability to describe various relations. These various relations may be attributed to the natural resistance of the corrugation geometry itself to the applied load during crushing process. Generally, the corrugation angle α plays a significant role in the energy absorption capacity of frusta.

8. Effect of the frustum length-to-thickness ratio L/t

six finite element corrugated models of different length-to-thickness ratio L/t ranged from 50 to 250 were examined. It is found that decreasing the length-to-thickness ratio L/t causes a significant increase in the amount of energy absorbed by models. The accumulative energy absorbed by different L/t corrugated frusta is assessed at various deformation levels. The energy-displacement curves are calculated by integrating the area under the obtained load-displacement curves. It is observed that all frustum models have a similar load-displacement characteristics and the energy absorption capacity increases with increasing deformation level. Furthermore, similar behaviour of the load-displacement curves in Fig.(6) reveals and confirms the similarity of the collapse mechanisms of frustum models independent of the frustum length-to-thickness ratio L/t.

Conclusion

The quasi-static axial loading of corrugated aluminum frusta compressed between two parallel flat rigid plates is investigated numerically by using the finite element code ABAQUS/Explicit. ABAQUS succeeded to simulate the multi-lobe and inward inversion failure mode of the straight frustum compared with the experimental one. However, the collapse mechanism of the corrugated frustum model is predicted in an axi-symmetric accordion failure mode, independent of the number of corrugations. The predicted load-displacement curve of each corrugated frustum model has a number of peaks equal to the number of corrugations of the investigated model. The amount of energy absorbed by the 25 corrugations frustum is highly greater than that absorbed by the 5 corrugations one. In other words, increasing the number of corrugations will increase the energy absorption capacity of the corrugated frusta. Crushing behaviour of the corrugated frustum is significantly affected by the corrugation angle α. The axial length-to-thickness ratio L/t plays an effective role in enhancement the energy absorbed by the corrugated frusta. Decreasing the ratio of L/t increases the energy absorption capacity of the corrugated frustum models.

References

[1] Alghamdi, A.A.A., “Collapsible Impact Energy Absorbers: an Overview”, Thin-Walled Structures, Vol. 39, pp. 189-213, 2001.
[2] Mamalis A. G. and Johnson W., “The Quasi-static crumpling of thin walled circular cylinders and frusta under axial compression”, Int. J. Mech. Sci., Vol. 25, No. 9, pp. 713-732, 1983.
[3] Mamalis A.G., Johnson W. and Viegelahn G. L., “The crumpling of steel thin-walled tubes and frusta under axial compression at elevated strain-rate: some experimental results”, Int. J. Mech. Sci., Vol. 26, No. 11/12, pp. 537-547, 1984.
[4] Mamalis A. G., Manolakos D.E., Saigal S., Viegelahn G. and Johnson W., “Extensible plastic collapse of thin-wall frusta as energy absorbers”, Int. J. Mech. Sci., Vol. 26, No. 4, pp. 219-229, 1986.
[5] Mamalis A. G., Manolakos D. E., Viegelahn G.L., Vaxevanidis N.M. and Johnson W., “On the axial collapse of thin-walled PVC conical shells”, Int. J. Mech. Sci., Vol. 28, No. 6, pp. 323-335, 1986.
[6] Mamalis A. G., Manolakos D. E., Viegelahn G. L. and Johnson W., “The modelling of the progressive extensible plastic collapse of thin-wall shells”, Int. J. Mech. Sci., Vol. 30, No. 3/4, pp. 249-261, 1988.
[7] El-Sobky H. and Singace A. A., “An Experiment on Elastically Compressed Frusta”, Thin-Walled Structures, Vol. 33, No. 4, pp. 231-244, 1999.
[8] El-Sobky H., Singace A. A. and Petsios M., “Mode of Collapse and Energy Absorption Characteristics of Constrained Frusta under Axial Impact Loading”, Int. J. Mech. Sci., Vol. 43, No. 3, pp. 743-757, 2001.
[9] Singace A. A., El-Sobky H. and Petsios M., “Influence of End Constraints on the Collapse of Axially Impacted Frusta”, Thin-Walled Structures, Vol. 39, pp. 415-428, 2001.
[10] Hibbitt H. D., Karlsson B. I. and Sorenson Inc., “ABAQUS/Explicit User’s Manual, Version 6.4”, 2003.

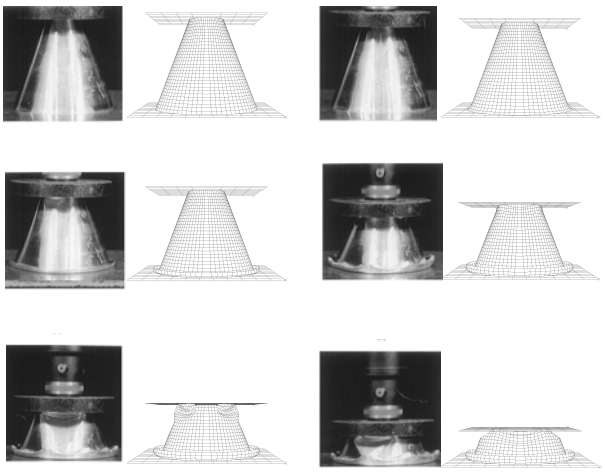

Fig.(1) Gradual crushing of the top constrained straight frustum using the present ABAQUS solution and the experimental results in Ref.[8]

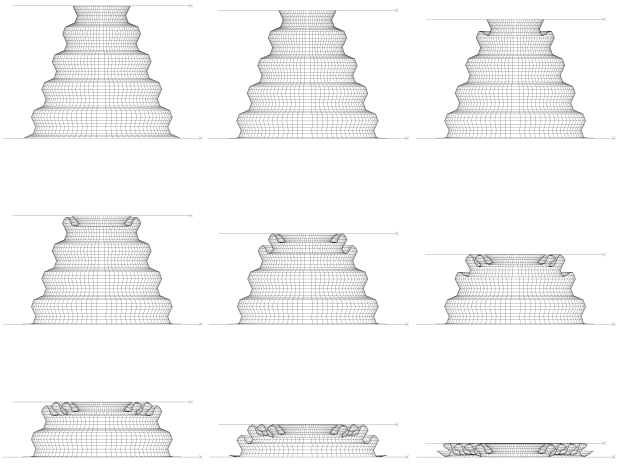

Fig.(3) Collapse mechanism of the 5 corrugations frustum model

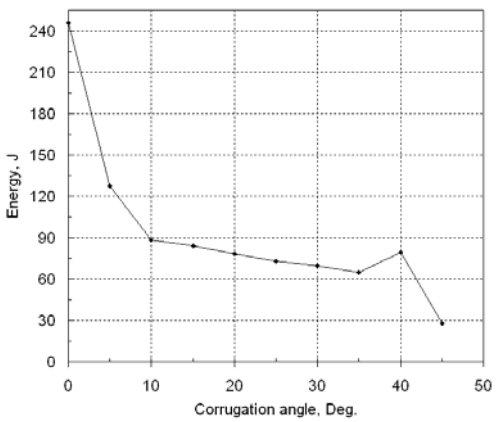

Fig.(5) Effect of the corrugation angle on the energy absorption capacity

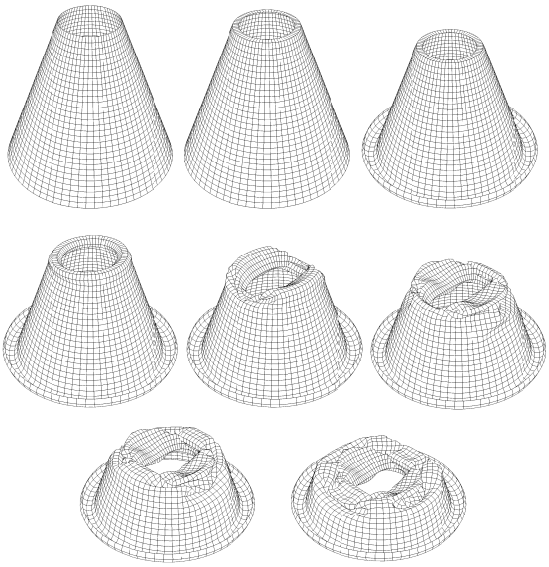

Fig.(2) Collapse mechanism of the straight frustum model

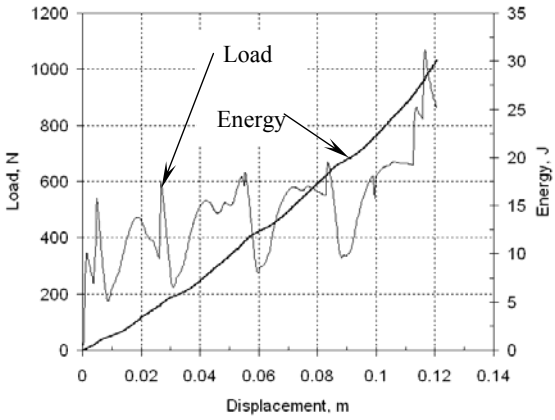

Fig.(4) Load- and energy-displacement curves of the 5 corrugations frustum model

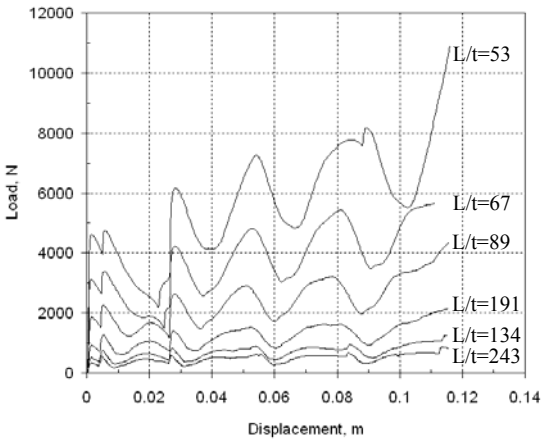

Fig.(6) Effect of the axial length-to-thickness ratio L/t on the load-displacement characteristics